A POD-selective inverse distance weighting method for fast parametrized shape morphing

note finali coverpage

(Article begins on next page)

15 May 2024

A POD-selective inverse distance weighting method for fast parametrized shape morphing

Francesco Ballarin[1], Alessandro D'Amario[1,2], Simona Perotto[3], and Gianluigi Rozza[1]

[1]mathLab, Mathematics Area, SISSA, via Bonomea 265, I-34136 Trieste, Italy
[2]Politecnico di Milano, via Giuseppe La Masa, 34, I-20156 Milano, Italy
[3]MOX - Modeling and Scientific Computing, Dipartimento di Matematica, Politecnico di Milano, piazza Leonardo da Vinci 32, I-20133 Milano, Italy

November 5, 2018

Abstract

Efficient shape morphing techniques play a crucial role in the approximation of partial differential equations defined in parametrized domains, such as for fluid-structure interaction or shape optimization problems. In this paper, we focus on Inverse Distance Weighting (IDW) interpolation techniques, where a reference domain is morphed into a deformed one via the displacement of a set of control points. We aim at reducing the computational burden characterizing a standard IDW approach without significantly compromising the accuracy. To this aim, first we propose an improvement of IDW based on a geometric criterion which automatically selects a subset of the original set of control points. Then, we combine this new approach with a dimensionality reduction technique based on a Proper Orthogonal Decomposition of the set of admissible displacements. This choice further reduces computational costs. We verify the performances of the new IDW techniques on several tests by investigating the trade-off reached in terms of accuracy and efficiency.

1 Introduction

Shape morphing plays a meaningful role in several engineering and life science fields, such as, for instance, aero-elasticity [41], high performance boat design [32, 31], modelling of the cardio-vascular system [4, 36]. On one hand, the same physical problem may involve the deformation of the domain, for instance, when dealing with fluid-structure interaction problems [8]. On the other hand, several applications imply iterative procedures where the same problem is solved in different geometric configurations. This is the case, e.g., of a multi-query context, such as shape optimization problems, where the shape of the domain is varied until a prescribed cost functional is minimized (or maximized) [44].

Our interest is focused on partial differential equations solved in a domain which changes in time. In such a case, the goal becomes twofold, since we aim to accurately approximate the domain as well as the partial differential equation. In general, it is not computationally affordable to generate a new discretization (mesh) of the domain at each deformed configuration. Indeed, mesh generation may be a time consuming procedure (both in terms of CPU time and assembling) and, sometimes, it is not directly integrated in the solver at hand. Therefore, it is often more convenient to generate a mesh for a reference configuration and then to morph it into the deformed grid. This work can be framed in such a context.

Several shape morphing techniques are available in the computer graphics community. A reference mesh is deformed by displacing some points (the so-called control points); then the shape morphing map associated with these points is applied to the whole discretized domain, thus avoiding any remeshing. These techniques have been recently applied to parametrized partial differential equations (PPDEs). For instance, shape morphing techniques based on *Free*

Form Deformation (FFD) [42] and *Radial Basis Functions* (RBF) interpolation [12] have been successfully applied to PPDEs [30, 34, 46], shape optimization problems [6, 45, 47], reconstruction of scattered geometrical data [18], mesh motion and interface coupling for fluid-structure interaction problems [10, 21, 23], interpolation between non-conforming meshes [19], sensitivity analysis studies in complex geometrical configurations [5].

In this paper we focus on a different approach, the *Inverse Distance Weighting* (IDW) interpolation that relies on the inverse of a weighted sum of distances between mesh nodes, some of which will be chosen as control points [43, 52, 53, 22].

A proper choice of the control points is a crucial step independently of the adopted morphing technique. A first requirement is to keep the number of control points as small as possible, since the complexity of the morphing map evaluation increases as the number of control points becomes larger. Such selection is usually driven by a prior knowledge of the phenomenon at hand. In some cases an automatic selection can be carried out. For instance, a sensitivity analysis to the control points is proposed for shape optimization problems in [6], where the control points selected are the ones providing the largest variation of a cost functional. Local minima and maxima of structure eigenmodes are employed in [23] as control points to perform mesh motion in fluid-structure interaction problems.

Here, we propose a variant of the IDW method that combines the shape morphing procedure with a new criterion to select the control points based on geometrical considerations and, consequently, independently of the underlying partial differential equations. We will refer to this variant as to Selective IDW (SIDW) approach.We remark that the Selective methodology proposed in this work for IDW can be applied to RBF and to improved variants of FFD, such as the one based on NURBS functions[1] [29]. We further reduce the computational cost of morphing by applying dimensionality reduction to the deformations associated with shape morphing. In particular, thanks to the employment of a reference domain, we identify any shape deformation with a certain parametric configuration of the original structure, the parameter being strictly related to the control point displacement. This suggests us to resort to a dimensionality reduction approach, and we choose, in particular, the Proper Orthogonal Decomposition (POD). We will refer to this combined technique as to POD-SIDW. POD, also known as Principal Component Analysis (PCA), is used in the literature, for instance, in statistical shape analysis [20], as well as for mesh deformation and optimization [3, 50]. Manifold learning techniques are combined with PCA for efficient structural shape optimization in [37]. An equivalent shape representation by means of currents is sought in [48] in order to introduce an Hilbert space over shapes and apply PCA. Application to life sciences of PCA has been proposed in [26, 35].

The paper is organized as follows. In Section 2, after formalizing the standard approach, we set the selective variant of IDW interpolation. Both the approaches are customized in a shape morphing setting and numerically compared on structural configurations of interest in aeronautic and naval engineering. Section 3 deals with dimensionality reduction. POD is directly applied to the selective IDW interpolation and the numerical benefits due to such a merging of techniques are investigated when dealing with shape morphing. Some conclusions are finally drawn in Section 4 together with perspectives for a future development of the present work.

2   Inverse Distance Weighting techniques

In this section, we consider two techniques to drive a shape morphing process, with particular interest in fluid-structure interaction (FSI) problems. In this context, a mesh motion is performed to extend the structural displacement (computed with an appropriate structural model) into the fluid, resulting in a morphed fluid domain. In particular, we first introduce the original Inverse Distance Weighting (IDW) interpolation, and then we propose a new variant of this method to overcome some of its intrinsic computational limits.

---

[1]Control points are constrained to a lattice in the original FFD approach [42], while later FFD variants, such as the NURBS-FFD method, allow a greater freedom in the control point selection.

2.1 The Inverse Distance Weighting (IDW) approach

The IDW method has been originally proposed in [43] to deal with two-dimensional interpolation problems, and successively extended to higher-dimensional and applicative settings (see, e.g., [15, 33, 53, 52]).

Let $\Omega_r \subset \mathbb{R}^d$, with $d = 1, \ 2, 3$, be the reference domain, and let $u : \Omega_r \to \mathbb{R}$ be a continuous function. We select a prescribed set $\mathcal{C} = \{\mathbf{c}_k\}_{k=1}^{\mathcal{N}_c}$ of points in Ω_r, known as *control points*. Then, the *IDW interpolant* of u, $\Pi_{\text{IDW}}(u)$, coincides with the continuously differentiable function

$$\Pi_{\text{IDW}}(u)(\mathbf{x}) = \sum_{k=1}^{\mathcal{N}_c} w_k(\mathbf{x})\, u(\mathbf{c}_k) \quad \mathbf{x} \in \Omega_r, \tag{1}$$

where the local weight functions $w_k : \Omega_r \to \mathbb{R}$, for $k = 1, \dots, \mathcal{N}_c$, are defined by

$$w_k(\mathbf{x}) = \begin{cases} \dfrac{\|\mathbf{x} - \mathbf{c}_k\|^{-p}}{\displaystyle\sum_{j=1}^{\mathcal{N}_c} \|\mathbf{x} - \mathbf{c}_j\|^{-p}} & \text{if } \mathbf{x} \neq \mathbf{c}_k, \\ 1 & \text{if } \mathbf{x} = \mathbf{c}_k, \\ 0 & \text{otherwise,} \end{cases} \tag{2}$$

with $\|\cdot\|$ the standard Euclidean norm, and for some positive integer p. Notice that weights are automatically selected such that the influence of the k-th control point $\mathbf{c}_k$ on $\mathbf{x}$ diminishes as the distance between $\mathbf{x}$ and $\mathbf{c}_k$ increases. Power p tunes such an inverse dependence, so that the weight assigned to a point $\mathbf{x}$ far from the control points becomes smaller and smaller as p increases. With reference to FSI problems, the choice of parameter p is crucial to avoid compenetration effects between fluid and structure [52].

2.1.1 IDW for shape morphing

To set shape morphing into the IDW interpolation framework, we identify the reference domain Ω_r with the initial configuration of the physical domain. Then, we consider a discretization $\Omega_h = \{\mathbf{x}_i\}_{i=1}^{\mathcal{N}_h} \subset \Omega_r$, with $\mathbf{x}_i$ being all the nodes of the mesh, and we identify function u in (1) with the deformation d of points $\mathbf{x}_i$ and the set $\mathcal{C}$ of the control points (also denoted as parameters) with a subset of Ω_h. In such a context, the IDW interpolant, $\Pi_{\text{IDW}}(d)$, represents the so-called *shape parametrization map*.

The choice of the control points clearly represents a crucial issue. In general, $\mathcal{C} \subset \Omega_h$ coincides with the set of the boundary points of Ω_h. This is a common practice in several engineering applications, in particular, in FSI problems, where the displacement is prescribed at the interface between fluid and structure and, successively, extended to the interior of the fluid to identify the deformed fluid domain, Ω_d [9, 13, 38].

To formalize shape morphing in a more computationally practical way, we collect the displacements[2] assigned at the control points in the vector $\mathbf{d}_c \in \mathbb{R}^{\mathcal{N}_c}$, with $[\mathbf{d}_c]_i = d(\mathbf{c}_i)$ and $i = 1, \dots, \mathcal{N}_c$. In practice, values $d(\mathbf{c}_i)$ are often constrained to suitable ranges in order to satisfy admissible shape configurations (see, e.g., [30]). Then, the deformation $\mathbf{d} \in \mathbb{R}^{\mathcal{N}_h}$ of points $\mathbf{x}_i$ in Ω_h, with $[\mathbf{d}]_i = d(\mathbf{x}_i)$ and $i = 1, \dots, \mathcal{N}_h$, is computed via the IDW interpolant (1)-(2) as

$$\mathbf{d} = W \mathbf{d}_c, \tag{3}$$

with $W \in \mathbb{R}^{\mathcal{N}_h \times \mathcal{N}_c}$ the IDW matrix of generic component

$$W_{ik} = w_k(\mathbf{x}_i) \quad \text{for } i = 1, \dots \mathcal{N}_h \text{ and } k = 1, \dots, \mathcal{N}_c. \tag{4}$$

The matrix W keeps track of the internal structure of Ω_h, recording the reciprocal distance between control and internal points. For this reason, the IDW matrix is computed before morphing takes place, once and for all. The actual motion is imposed by vector $\mathbf{d}_c$, which, vice versa,

---

[2]In the following we will use the word *displacement* to address the input to the deformation process, and the word *deformation* to address the output of the deformation process.
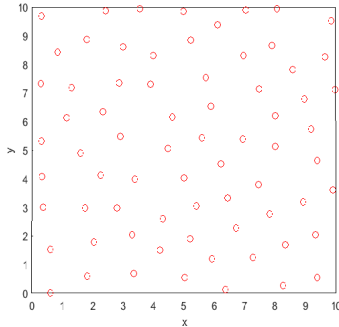
Figure 1: SIDW algorithm: distribution of control points after the selection process on the square $\Omega_r = (0, 10)^2$, being $\omega \equiv \Omega_r$.

varies during the morphing process in order to follow the shape deformation. Finally, vector $\mathbf{d}$ identifies a discretization of the deformed domain Ω_d.

Relation (3) highlights the ease of implementation of a morphing strategy driven by IDW interpolation. In particular, when applied to FSI configurations, this approach provides a sharp description of the interface displacement, by properly tackling also portions of the domain characterized by a null displacement and by avoiding compenetrations effects. Additionally, a good mesh quality is usually guaranteed (we refer to Section 2.3 for more details), even in the presence of large deformations.

Nevertheless, the standard IDW approach does not prescribe, a priori, any smart criterion to select the control points. The value $\mathcal{N}_c$ may consequently become very large, especially in the presence of practical configurations, so that the computational effort required by the assembly and by the storage of matrix W may be very massive. Matrix $W \in \mathbb{R}^{\mathcal{N}_h \times \mathcal{N}_c}$ is actually dense, and its storage may lead to extremely high memory requirements. This justifies the proposal of the new IDW formulation in the next section, where a new set $\widehat{\mathcal{C}}$ of control points is properly selected via an automatic procedure, so that $\text{card}(\widehat{\mathcal{C}}) \ll \mathcal{N}_c$, $\text{card}(\mathcal{S})$ denoting the cardinality of the generic set $\mathcal{S}$. Sparsification of matrix W provides an alternative way to reduce the computational burden of IDW [39, 40], though this is beyond the scope of this work. Notice that the method proposed here is complementary to a sparsification approach, so that the two approaches can be, in principle, combined to further reduce the computational effort.

2.2 The Selective Inverse Distance Weighting (SIDW) approach

The new procedure proposed in this section aims at reducing the computational effort demanded by the standard IDW interpolation. In particular, since the most computationally demanding part of the IDW algorithm is the memory storage, we aim at reducing the number of control points by automatically selecting the most relevant points in $\mathcal{C}$ to sharply describe the initial configuration Ω_h as well as the deformed domain Ω_d. For this reason, we refer to the new approach as to the Selective IDW (SIDW) formulation.

The starting point is the approach proposed in [43] which is essentially suited to deal with regimes of small deformations. Our goal is to improve this procedure to tackle also large displacement configurations, without violating the no-compenetration constraint. Additionally, we aim at guaranteeing a uniform distribution in the reduced set of control points.

The complete SIDW procedure is provided by **Algorithm 1**. To set notation, we denote by: $\widehat{\mathcal{C}} = \{\widehat{\mathbf{c}}_j\} \subset \mathcal{C}$ the subset of the selected control points; $\omega \subseteq \Omega_r$ the region where the selection is applied; $R > 0$ the selection radius; $B(\mathbf{c}; r)$ the ball of center $\mathbf{c}$ and radius $r > 0$; $B(\mathbf{c}; r_i, r_e)$ the circular annulus of center $\mathbf{c}$, inner radius r_i and outer radius r_e, with $r_e > r_i > 0$.

We first exemplify the action of the SIDW procedure starting from a configuration characterized by $\Omega_r = (0, 10)^2$ and $\omega \equiv \Omega_r$. Then, we will particularize such a procedure to a shape morphing setting.

SIDW algorithm consists essentially of two phases, i.e., an *initialization* phase and the actual *selection* phase. Now, let $\widehat{\mathbf{c}}_1 \in \mathcal{C}$ be a randomly selected control point.

The goal of the initialization phase is to perform a tessellation of the region $\omega \setminus B(\widehat{\mathbf{c}}_1; R)$ via

n concentric annuli, $\{\alpha_m\}_{m=1}^n$, of thickness aR (lines 2-7), being $a \in \mathbb{R}$ a positive constant picked by the user, with $a < 1$. Concerning the specific example on the square $\Omega_r = (0,10)^2$, we refer to Figure 2(a), where the tessellation corresponding to $R = 2.1$ and $a = 0.8$ is shown, the control point $\widehat{\mathbf{c}}_1$ being marked in the plot. To simplify the graphical representation, we highlight only the control points constituting $\widehat{\mathcal{C}}$. Four annular regions are identified by the choice done for the input parameters, thus inducing a partitioning of the original control points in $\mathcal{C}$. Then, all the control points in $\mathcal{C}$ belonging to the *area of influence*, $B(\widehat{\mathbf{c}}_1; R)$, around $\widehat{\mathbf{c}}_1$ are removed from $\mathcal{C}$. This operation concludes the first phase of SIDW algorithm.

Algorithm 1 : SIDW interpolation

1: **function** SIDW(ω, $\mathcal{C}$, $\widehat{\mathbf{c}}_1$, R, a, b, u)
2:      $n \leftarrow 1$, $r \leftarrow R$, $r_\omega \leftarrow \min\{r > 0 : \omega \supseteq B(\widehat{\mathbf{c}}_1; r)\}$
3:      **while** $r \leq r_\omega$ **do**
4:          $\alpha_n \leftarrow B(\widehat{\mathbf{c}}_1; r, r + aR) \cap \mathcal{C}$
5:          $r \leftarrow r + aR$
6:          $n \leftarrow n + 1$
7:      **end while**
8:      $k \leftarrow 1$, $m \leftarrow 1$, $\beta \leftarrow \alpha_1 \cap B(\widehat{\mathbf{c}}_1; R, bR)$
9:      **while** $m \leq n$ **do**
10:          **while** $\beta \neq \emptyset$ **do**
11:              $\widehat{\mathbf{c}}_{k+1} \leftarrow$ SelectControlPoint(β)
12:              **for** $l = m, \ldots, n$ **do**
13:                  $\alpha_l \leftarrow \alpha_l \setminus B(\widehat{\mathbf{c}}_{k+1}; R)$
14:              **end for**
15:              $\beta \leftarrow \alpha_m \cap B(\widehat{\mathbf{c}}_{k+1}; R, bR)$
16:              $k \leftarrow k + 1$
17:          **end while**
18:          **if** $\alpha_m = \emptyset$ **then**
19:              $\beta \leftarrow \alpha_{m+1} \cap B(\widehat{\mathbf{c}}_k; R, bR)$
20:              $m \leftarrow m + 1$
21:          **else**
22:              $\beta \leftarrow \alpha_m$
23:          **end if**
24:      **end while**
25:      $\widehat{\mathcal{C}} \leftarrow \{\widehat{\mathbf{c}}_j\}_{j=1}^k$
26:      computation of $\Pi_{\text{SIDW}}(u)$
27: **end function**

The selection phase begins with a first initialization of the *area of selection*, β, around the first control point $\widehat{\mathbf{c}}_1$, defined as the intersection between α_1 and the circular annulus $B(\widehat{\mathbf{c}}_1; R, bR)$, with $b > 1$ a user defined positive constant (line 8). Then, a loop on the annular regions $\{\alpha_m\}_{m=1}^n$ of the tessellation is started (line 9). Inside this loop, until β is empty, a new control point is selected in β via the SelectControlPoint function (line 11). Then, all the control points in $\mathcal{C}$ belonging to each area of influence α_l around the current control point $\widehat{\mathbf{c}}_{k+1}$ are removed (lines 12-14), and a new area of selection β is computed as the intersection between the current area of influence α_m and a circular annulus $B(\widehat{\mathbf{c}}_{k+1}; R, bR)$ (line 15).

Concerning function SelectControlPoint, different criteria can be implemented to select the new control point $\widehat{\mathbf{c}}_{k+1}$. For instance, a geometric selection can be applied by picking the control point closest to the centroid of β or the farthest control point with respect to the already selected points in $\widehat{\mathcal{C}}$. To simplify the procedure, in the numerical assessment below, we resort to a random choice of $\widehat{\mathbf{c}}_{k+1}$ in β.

Figure 2(b) displays the firstly initialized area of selection β, together with the second control point $\widehat{\mathbf{c}}_2$, being $b = 1.4$. The remaining panels in Figure 2 show the effects of the successive removals operated by the while loop. Six iterations are associated with the first area of influence α_1. In particular, the new area of selection β and the corresponding control point $\widehat{\mathbf{c}}_{k+1}$ associated with the first two (Figure 2(c)-(d)) and the last (Figure 2(e)) removals are highlighted.

When β is empty, a re-initialization of the area of selection is performed (`lines 18-23`). If the current annulus α_m is exhausted, then the area of selection is sought in the next annulus, α_{m+1}, (`lines 19-20`). Figure 2(f) shows the transition from α_1 to α_2. Additionally, `line 22` handles the very peculiar case when α_m is not actually exhausted, yet it is disconnected from the area of selection around the current control point $\widehat{\mathbf{c}}_{k+1}$. In such a case, β is simply reset to α_m.

Finally, once all the circular annuli in the tessellation $\{\alpha_m\}_{m=1}^n$ are exhausted, SIDW algorithm ends, and the new set $\widehat{\mathcal{C}}$ of selected control points is returned (`line 25`). The final distribution of control points for the considered specific configuration on the square $\Omega_r = (0, 10)^2$ is provided in Figure 1. The selected points are uniformly distributed as desired. At this point, the *SIDW interpolant* of u, $\Pi_{\mathrm{SIDW}}(u)$, can be computed (`line 26`) as

$$\Pi_{\mathrm{SIDW}}(u)(\mathbf{x}) = \sum_{k=1}^{\mathcal{N}_{\widehat{c}}} w_k(\mathbf{x}) \, u(\widehat{\mathbf{c}}_k) \quad \mathbf{x} \in \Omega_r, \tag{5}$$

with $\mathrm{card}(\widehat{\mathcal{C}}) = \mathcal{N}_{\widehat{c}} \ll \mathcal{N}_c$, and where the weight functions w_k are defined according to (2) having replaced $\mathbf{c}_k$ with $\widehat{\mathbf{c}}_k$.

A few remarks are in order. The three input parameters, R, a and b, tune the SIDW algorithm and, as a consequence, the final selection $\widehat{\mathcal{C}}$ of control points. In particular, they vary the area of the annular regions $\{\alpha_m\}_{m=1}^n$, as well as of the areas of influence and selection. In more details, concerning the radius R, it turns out that the smaller R, the larger the number of selected control points. As far as a and b are concerned, smaller values of a lead to a larger number n of annular regions α_m, which generally results in a finer control point distribution; larger values of b leads to larger areas of selection β, resulting in a smaller number of selected control points. The choice of R, a and b as well as the corresponding interplay is difficult to be established *a priori* and, clearly, it is problem-dependent. A sensitivity analysis of SIDW with respect to these parameters will be carried out in Section 2.3.

Finally, we remark that, especially in practical applications, it might be advisable to split ω into smaller subregions, ω_p, and to use various values for the parameters R, a and b to tackle possible local different discretizations.

2.2.1 SIDW for shape morphing

Now we customize SIDW algorithm to manage shape morphing. We consider the discretization $\Omega_h = \{\mathbf{x}_i\}_{i=1}^{\mathcal{N}_h}$ of the initial configuration of the physical domain and we assume to know the displacement d at each control point $\mathbf{c}_k \in \mathcal{C}$, for $k = 1, \ldots, \mathcal{N}_c$. We remind that, in such a case, $\mathcal{C}$ is a subset of boundary nodes in Ω_h.

Our idea consists in deforming each boundary node of Ω_h according to the deformation prescribed at $\{\mathbf{c}_k\}_{k=1}^{\mathcal{N}_c}$, while selecting a subset of control points to update the deformation of the internal nodes of Ω_h.

For this purpose, we resort to the procedure itemized in **Algorithm 2**, following a selection-deformation paradigm.

During the selection phase, which is performed once and for all, we first filter set $\mathcal{C}$ via the selection procedure in **Algorithm 1**, to obtain the subset $\widehat{\mathcal{C}}$ of control points $\widehat{\mathbf{c}}_k$, with $k = 1, \ldots, \mathcal{N}_{\widehat{c}}$ (`item (i)`), using $\omega = \partial\Omega_r$, a random point $\mathbf{c}_1 \in \mathcal{C}$ and considering the displacement as the variable u to be interpolated. Then, we build the SIDW matrix $\widehat{W}$ according (4) associated with $\widehat{\mathcal{C}}$ and with the set of the internal nodes of Ω_h (`item (iii)`). As an option, we can add to the filtered set $\widehat{\mathcal{C}}$ extra control points to include possible specific constraints to the problem (`item (ii)`). This occurs, for instance, when a null displacement is assigned to a portion of the domain. In such a case, the fixed nodes have to be necessarily included in the set $\widehat{\mathcal{C}}$. User-defined and problem-specific constraints may be added as well, for instance to attempt to avoid poor-quality and inverted elements in case some boundary points undergo a small deformation, whereas nearby boundary points are deformed significantly. In the sequel, we refer to this variant of the SIDW algorithm as to ESIDW (*Enriched* SIDW) interpolation.

The online phase performs the actual shape morphing. Each boundary node of Ω_h is deformed via the displacement assigned at the control points in $\mathcal{C}$ (`item (iv)`). Successively, we deform the internal nodes of Ω_h as
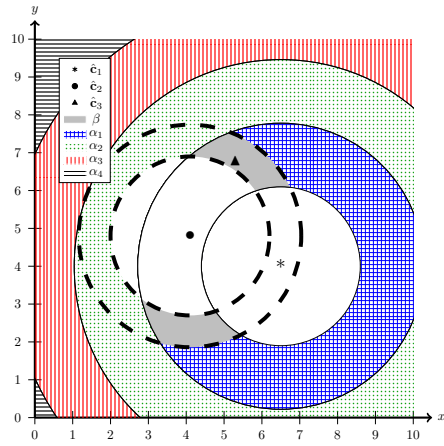
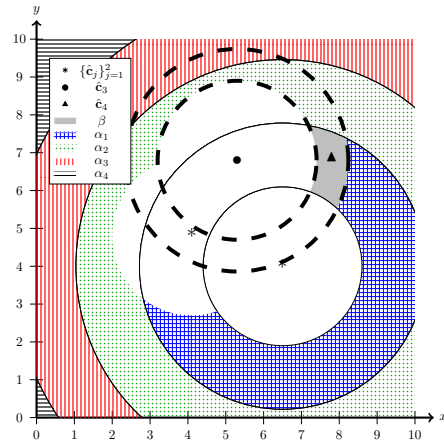$$\mathbf{d}^i = \widehat{W}\mathbf{d}_{\widehat{c}}, \tag{6}$$
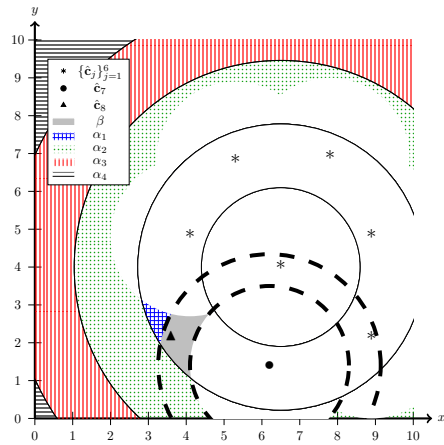
6
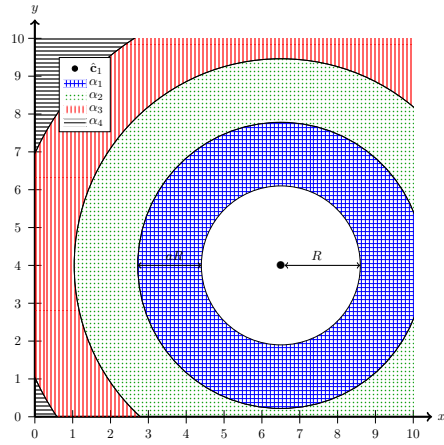
(a) Initialization phase.
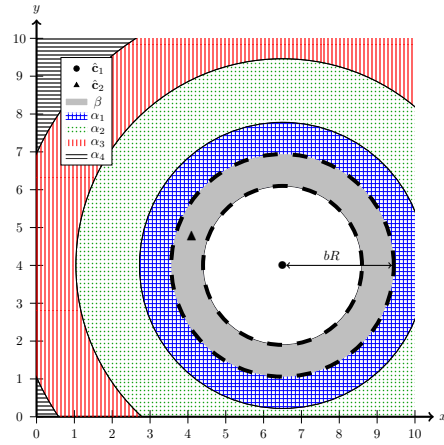
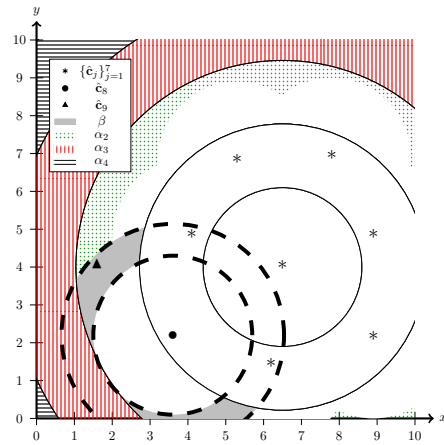(b) Selection phase: identification of β and of $\widehat{\mathbf{c}}_2$.

(c) Selection phase: first removal associated with α_1.

(d) Selection phase: second removal associated with α_1.

(e) Selection phase: sixth removal associated with α_1.

(f) Selection phase: first removal associated with α_2.

Figure 2: SIDW algorithm: initialization (a) and first iterations (b)-(f) of the selection phase applied to the square $\Omega_r = (0,10)^2$, being $\omega \equiv \Omega_r$.

7

where $\mathbf{d}^i \in \mathbb{R}^{\mathcal{N}_h^i}$ collects the deformation of the internal nodes, $\mathbf{x}_j$ for $j = 1, \ldots, \mathcal{N}_h^i$, of Ω_h, $\widehat{W} \in \mathbb{R}^{\mathcal{N}_h^i \times \mathcal{N}_{\widehat{c}}}$ is the (E)SIDW matrix computed in the offline phase, and $\mathbf{d}_{\widehat{c}} \in \mathbb{R}^{\mathcal{N}_{\widehat{c}}}$ is the vector of the displacements of the selected control points in $\widehat{\mathcal{C}}$ (`item (v)`).

Algorithm 2 can be advantageously exploited to deal with FSI problems. In such a case, we identify domain Ω_r with the fluid domain. The displacement of the interface is generally provided by a structure solver, so that it suffices to compute the deformation of the fluid nodes via the procedure detailed in the algorithm.

Algorithm 2 SIDW interpolation for shape morphing

SELECTION PHASE:

    (i) apply the selection procedure in **Algorithm 1** to $\mathcal{C}$ to extract the subset $\widehat{\mathcal{C}}$;

    (ii) *Optional [ESIDW method]* : add to the set $\widehat{\mathcal{C}}$ extra control points to account for problem constraints;

    (iii) assemble the SIDW matrix $\widehat{W}$ associated with $\widehat{\mathcal{C}}$ and with the internal nodes of Ω_h.

DEFORMATION PHASE:

    (iv) deform boundary nodes of Ω_h via the displacement assigned at the control points in $\mathcal{C}$;

    (v) deform internal nodes of Ω_h according to (6).

2.3 IDW versus SIDW interpolation

In this section we investigate the performances of IDW and SIDW interpolation algorithm. In particular, we consider configurations of interest in aeronautic and naval engineering. We focus on 3D test cases and on tetrahedral meshes, although the procedure can be generalized to any dimension and to arbitrary meshes. Concerning the choice of the parameter p in (2), we set $p = 4$, essentially driven by numerical considerations. In all the test cases, we will consider a shape morphing process where the deformation is driven by an analytic law provided as input to **Algorithm 2**. As an alternative, we can employ a structural solver to compute the displacement to be assigned to the structure, but this is beyond the goal of this paper. To check the improvements led by the new approach, we compare IDW and SIDW interpolations in terms of computational effort. Both the procedures are implemented in the `C++` open source library `libMesh` [28], while the visualization software `ParaView` is employed for the post-processing of the solutions [2]. Concerning mesh generation, we resort to `SALOME` [1]. Finally, all the simulations are performed on a laptop with Intel® Core™ i7 CPU and 4GB RAM.

2.3.1 Structural deformation of a wing

We consider a wing characterized by a NACA0012 profile, clamped on the left side (see Figure 3, top). Table 1 gathers the main properties of the reference domain Ω_r and of the corresponding mesh Ω_h. We impose a vertical displacement to the boundary of the wing. In particular, denoting by z the distance from the clamped side and by y the vertical direction, we assign the displacement

$$\delta y = \delta y(z) = 0.01 z^2 \tag{7}$$

in the y direction (see Figure 3, bottom). The goal of this test case is to check the deformation capabilities of IDW and SIDW methods on a simple case of shape morphing, inspired by a possible application to shape optimization problems. The actual applicability to FSI problems (where mesh motion concerns the fluid domain) will be discussed in Section 2.3.2.

First, we apply the standard IDW approach, after identifying $\mathcal{C}$ with the set of all the boundary nodes of Ω_h (see Figure 4, top), so that the IDW matrix W in (3) belongs to $\mathbb{R}^{797 \times 1666}$. The resulting deformed wing, shown in Figure 3, bottom, is obtained after[3] 0.25 [s].

---

[3]Here and in the following, unless when referring to a specific phase of the deformation process, the time we refer to includes the time required by (3) as well as the time to update the mesh. For this reason, the actual speedup might be lower than the expected (ideal) one.
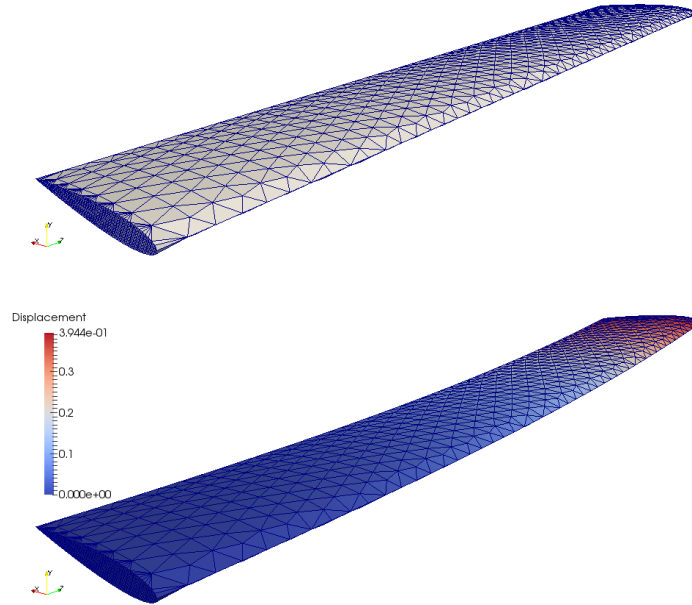
Figure 3: Structural deformation of a wing: reference (top) and IDW deformed (bottom) configuration.

longitudinal dimension	2π [m]
profile chord length	1.01 [m]
# elements	8850
# nodes	2463
# internal nodes	797
# boundary nodes	1666

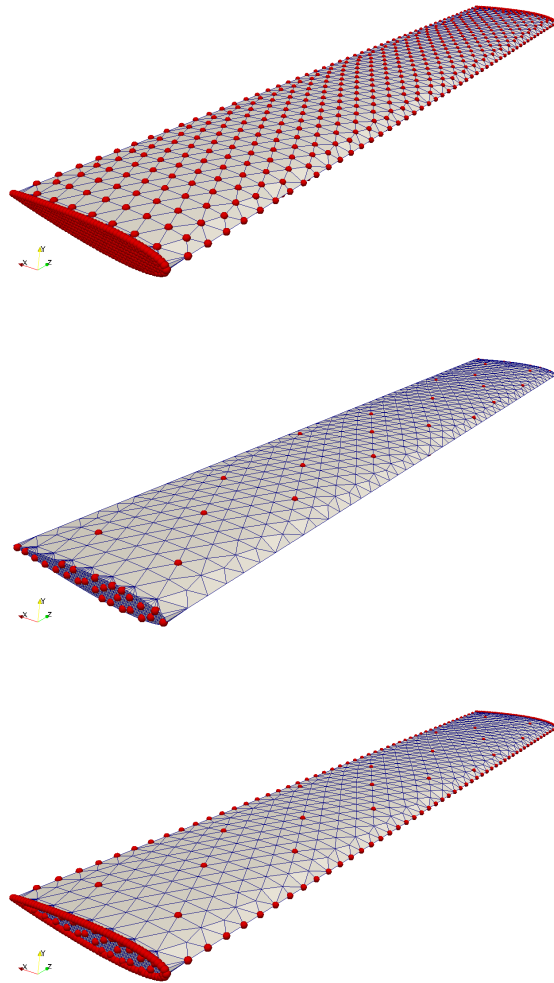Table 1: Structural deformation of a wing: main properties of Ω_r and of Ω_h.

Figure 4: Structural deformation of a wing: control points associated with the IDW (top), SIDW (center) and ESIDW (bottom) interpolation.
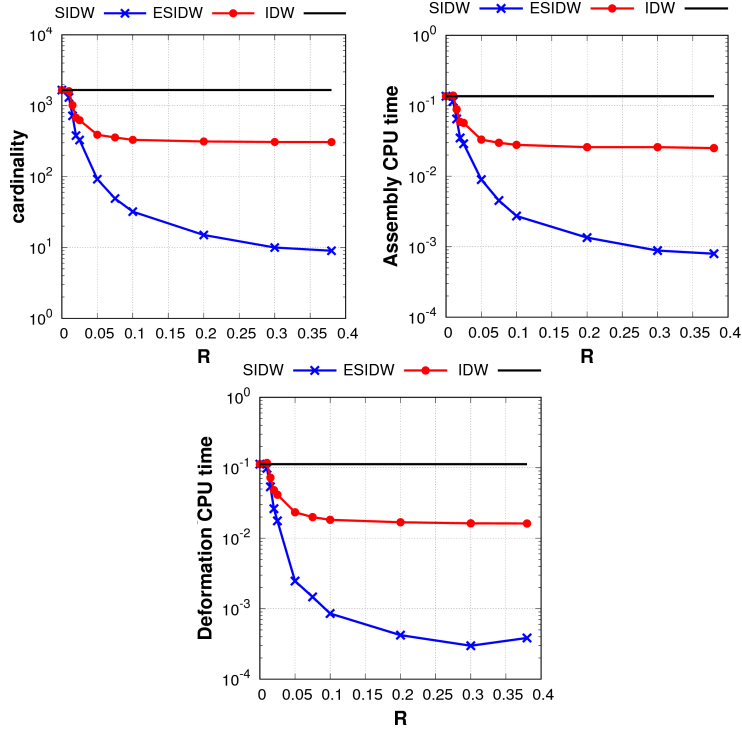
Figure 5: Structural deformation of a wing: cardinality of the control point set (left), assembly (center) and deformation (right) CPU time as a function of R.

We now resort to the SIDW interpolation algorithm. Set $\mathcal{C}$ still contains all the boundary nodes. We adopt two different values for the selection radius, i.e., $R = R_{lr} = 0.05$ [m] for the left and the right lateral surfaces of the wing, and $R = R_{tb} = 10 \cdot R_{lr} = 0.5$ [m] for the top and the bottom surfaces. Factor 10 is approximately the square root of the ratio, A_{tb}/A_{lr}, between the sum, A_{tb}, of the areas of the top and of the bottom surfaces of the wing, and the sum, A_{lr}, of the areas of the left and of the right sides. Finally, parameters a and b are set to 0.8 and 1.3, respectively.

We first employ the basic SIDW interpolation procedure, by skipping the enrichment step (ii) in **Algorithm 2**. Figure 4, center highlights the new set $\widehat{\mathcal{C}} \subset \mathcal{C}$, consisting of 92 control points. Notice the very coarse and uniform distribution of control points $\widehat{\mathbf{c}}_k$. The deformed configuration yielded by the SIDW approach essentially coincides with the one in Figure 3, bottom (see the analysis below for more quantitative investigations), despite a considerable reduction of the interpolation matrix, being $\widehat{W} \in \mathbb{R}^{797 \times 92}$, and of the corresponding computational time (the deformation phase takes only 0.015 [s]).

We successively resort to the ESIDW variant. We preserve the same values for a, b, R_{lr} and R_{tb} as in the previous numerical check. Additionally, we constrain the selection procedure to include in $\widehat{\mathcal{C}}$ all the nodes along the left and the right edge profiles of the wing as well as the nodes along the horizontal edges of the NACA profile. The rationale behind this choice is that control points acting on the left edge profile contribute with zero displacement in the interpolatory procedure. This results in a very small deformation for the neighboring internal points, thus preserving the continuity of the deformation, as the wing is clamped along that side. Moreover, since the displacement depends only on z, we expect that enforcing control points along horizontal edges (parallel to the z-axis) is instrumental to closely capture (with a small number of control points) the overall motion of the wing. Finally, control points are added along the right edge profile for symmetry. The enrichment increases the cardinality of $\widehat{\mathcal{C}}$, now consisting of 390 control points. As shown in Figure 4, bottom, all the nodes along the left and the right profiles of the wing are retained as control points, while the distribution of the control points on the top (and on the bottom) of the wing is essentially the same as in Figure 4, center. Also in this case the deformed configuration is essentially the same as the one in Figure 3, bottom (see the analysis below for
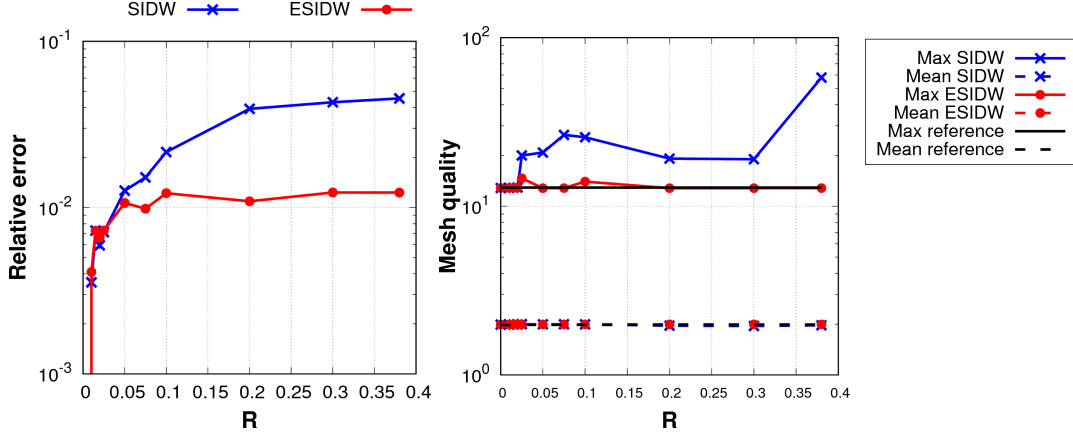
11

Figure 6: Structural deformation of a wing: relative error (left) and maximum and mean mesh quality (right) as a function of R.

more quantitative investigations). Concerning the computational time, the increased cardinality of $\widehat{\mathcal{C}}$ results in an deformation stage that takes 0.034 [s]. This time, despite larger than the one demanded by SIDW, is still one order of magnitude less with respect to the time required by the standard IDW interpolation.

Sensitivity to R. We investigate the sensitivity of SIDW and ESIDW interpolation to the selection radius. In particular, in Figure 5, we show the trend, as a function of R, of the number of the control points (left), and of the CPU time (in seconds) required to assemble the interpolation matrix (center) and to compute the deformation of the wing (right), respectively[4].
The relation between the number of control points and R is nonlinear for both the SIDW and ESIDW approaches. Nevertheless, while for the SIDW interpolation, the number of control points (and, consequently, the associated CPU time) increases as R becomes smaller, a low sensitivity to R is shown by the ESIDW variant. In particular, the cardinality of $\widehat{\mathcal{C}}$ remains the same for R greater than 0.1.
Concerning the CPU times, no significant difference distinguishes the trend associated with the matrix assembly and the deformation step, also quantitatively. As expected, ESIDW interpolation is more computationally demanding than the basic SIDW approach, whereas the standard IDW approach coincides with the most expensive procedure.

In Figure 6, left we show the error trend as a function of the selection radius. We compute the $L^2(\Omega_h)$-norm of the relative error between the SIDW (ESIDW) and the IDW deformation. The larger number of control points employed by the ESIDW interpolation yields more accurate deformations compared with the ones provided by the SIDW approach. In particular, for large enough values of R, the error due to SIDW is approximately 4%, while, for the ESIDW procedure, it is about 1%. Convergence to zero is guaranteed by both the methods as R decreases.

Finally, in Figure 6, right we investigate the influence of the selected radius R on the quality of the elements of the deformed meshes. Different criteria can be employed to quantify the mesh quality $\mathcal{Q}$. Here, we adopt the ratio between the longest and the shortest edge [24]. In the figure, for different values of R, we compare the maximum and the mean value of $\mathcal{Q}$ on the meshes generated by SIDW and ESIDW algorithms, with the corresponding values associated with the initial configuration Ω_h. While, on average, the mean value of $\mathcal{Q}$ is essentially independent of the deformation procedure and of the selected R, more sensitivity is appreciable on the maximum value of $\mathcal{Q}$. The sufficiently large number of control points allows ESIDW to preserve about the same value of $\mathcal{Q}$ as for the initial mesh, also when R increases. On the contrary, a deterioration on the maximum mesh quality is evident when dealing with the SIDW interpolation algorithm, especially for large values of R.

---

[4]In order to improve the reliability of these timings, the same deformation has been repeated 100 times. Thus, assembly and deformation CPU times provided in the figures correspond to the average. The standard deviation is less than 0.001 [s] in any case.

Sensitivity to a and b. We also study the sensitivity of the control point cardinality and of the accuracy of SIDW interpolation on the parameters a and b. Similar conclusions can be drawn for the ESIDW approach. To simplify this analysis, we relate a and b so that $b = 1/a$, we pick $a < 1$ (i.e., $b > 1$), and we consider four different values of the selection radius, namely, $R = 0.02, 0.05, 0.2$ and 0.3. Figure 7 collects the results of this check.

For $a \ll 1$ (i.e., $b \gg 1$), the number of selected control points becomes larger and larger, as expected, with a consequent increment of the CPU time. Nevertheless, this does not necessarily entail an improvement in terms of accuracy, especially for large values of R. Indeed, for $R = 0.2, 0.3$, choosing $a \approx 1$ (i.e., $b \approx 1$) reduces the number of control points of about one order of magnitude with respect to the choice $a \ll 1$ (i.e., $b \gg 1$), while only a slightly lower relative error is guaranteed (see Figure 7, right). On the contrary, when R is small (see Figure 7, left), decreasing a (i.e., increasing b) improves the accuracy. This is due the fact that, for these choices of a (b) and R, the SIDW procedure selects almost all the available control points.

Thus, since the actual goal of SIDW procedures, is to reduce the computational burden, we are essentially interested in sufficiently large values of R. This suggests us that the choice $a \approx 1$ (i.e., $b \approx 1$) ensures a reasonable trade-off between efficiency and accuracy to the morphing procedure.
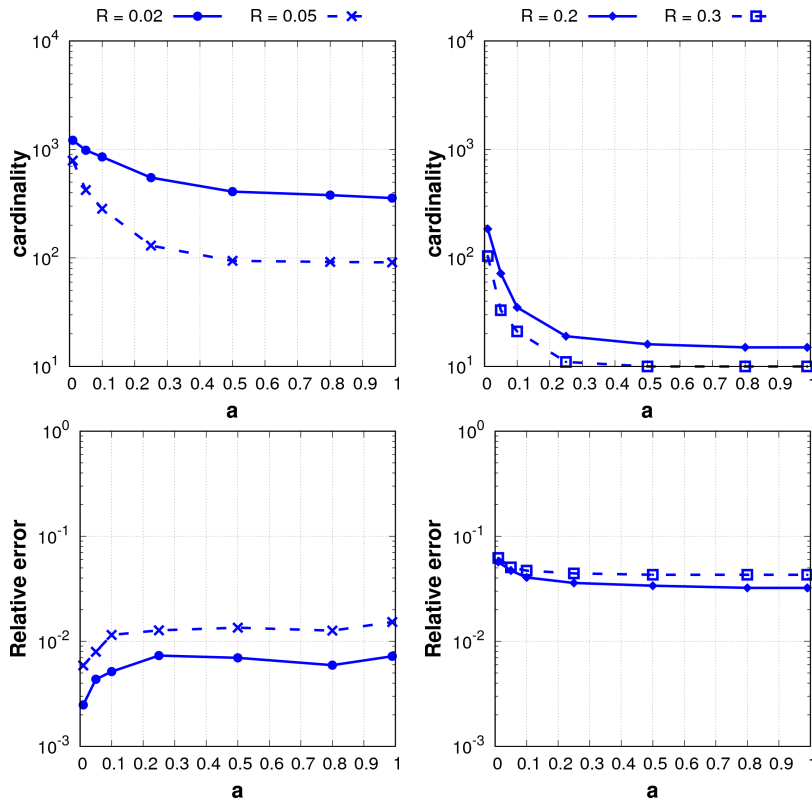

Figure 7: Structural deformation of a wing (SIDW interpolation): cardinality of the control point set (top) and $L^2(\Omega_h)$-norm of the relative error (bottom) as a function of a, for $R = 0.02, 0.05$ (left) and for $R = 0.2, 0.3$ (right).

Comparison with a random selection. We conclude this first test case by comparing the proposed selection procedure to a random control point selection, in terms of relative error. The random selection results from replacing step (i) in **Algorithm 2** with the following step:

(i') extract a random subset $\widehat{\mathcal{C}}_{\mathrm{rand}} \subset \mathcal{C}$.

The results of the comparison are shown in Figure 8, for SIDW (left) and ESIDW (right) procedures. We compare (as a function of R) the relative error attained by the SIDW (ES-IDW) selection with the average relative error over 100 random selections, each one such that

13

Without enrichment				With enrichment			
R	σ	$\Delta_{\min}$	$\Delta_{\max}$	R	σ	$\Delta_{\min}$	$\Delta_{\max}$
0.01	0.00031	-1.57	1.86	0.01	0.00047	-1.36	2.09
0.02	0.00073	-1.32	2.76	0.02	0.00084	-1.26	2.53
0.05	0.0018	-1.26	2.57	0.05	0.0013	-1.76	2.21
0.1	0.0043	-1.13	2.34	0.1	0.0017	-1.06	2.15
0.2	0.0072	-1.28	2.23	0.2	0.0014	-0.94	2.38
0.3	0.0091	-1.24	2.27	0.3	0.0012	-0.78	3.04

Table 2: Structural deformation of a wing: statistics for random selection procedure, without (left) and with (right) enrichment.

$\text{card}(\widehat{\mathcal{C}}_{\text{rand}}) = \text{card}(\widehat{\mathcal{C}})$. In particular, the area between the minimum and maximum error over the random selection is shaded. The error due to SIDW (ESIDW) is very close to the average error, thus resulting in a numerically equivalent way to compute the average approximation that can be achieved with $\text{card}(\widehat{\mathcal{C}})$ control points. We also remark that, for large values of R (i.e., for a very small number of control points), and especially for SIDW procedure, a random selection suffers from a large standard deviation σ (see Table 2). A large number of random selections (and correspondingly of deformations) may thus be required: SIDW and ESIDW turn out to be consequently more efficient procedure, as they require only one selection (i.e., a unique deformation). Finally, for what concerns the random selection, we denote by $\Delta_{\min}$ ($\Delta_{\max}$) the difference between the minimum (maximum) realized error and the average one, normalized to the standard deviation. As shown in Table 2, the resulting distribution is not symmetric, so that some random realizations return better configurations than the average one (to which the SIDW/ESIDW configuration is close to), since $|\Delta_{\min}| > 0$. However, they might also provide far worse configurations, being $\Delta_{\max} > |\Delta_{\min}|$. In particular, improvements are limited to the order of 1 standard deviation, while deteriorations can reach up to 3 standard deviations.
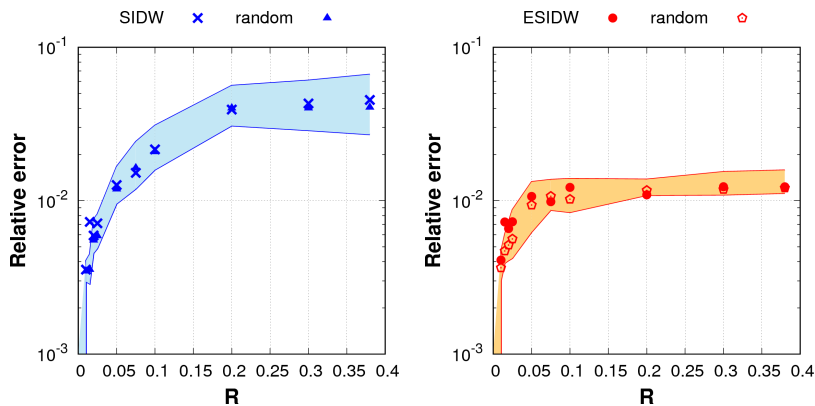

Figure 8: Structural deformation of a wing: comparison of relative errors for SIDW (left) and ESIDW (right) selection procedures to a random control point selection.

2.3.2 Fluid mesh motion around a wing

In this section we move to a FSI setting, by considering the fluid mesh motion around the NACA0012 profile in Figure 9, top. This test case mimics a typical study performed in a wind tunnel, where the wing is clamped on one side while, on the other side, it is deformed by a vertical displacement, such as the one in (7). Table 3 gathers the main properties of the physical domain and of the corresponding discretization.

To investigate the deformation in the fluid mesh, we start by applying the standard IDW approach, thus identifying the set $\mathcal{C}$ with all boundary nodes (see Figure 10, top for a detail in correspondence with the clamped side). The corresponding interpolation matrix in (3) belongs to $\mathbb{R}^{21910 \times 14126}$. The resulting deformed configuration, shown in Figure 9, bottom, is obtained
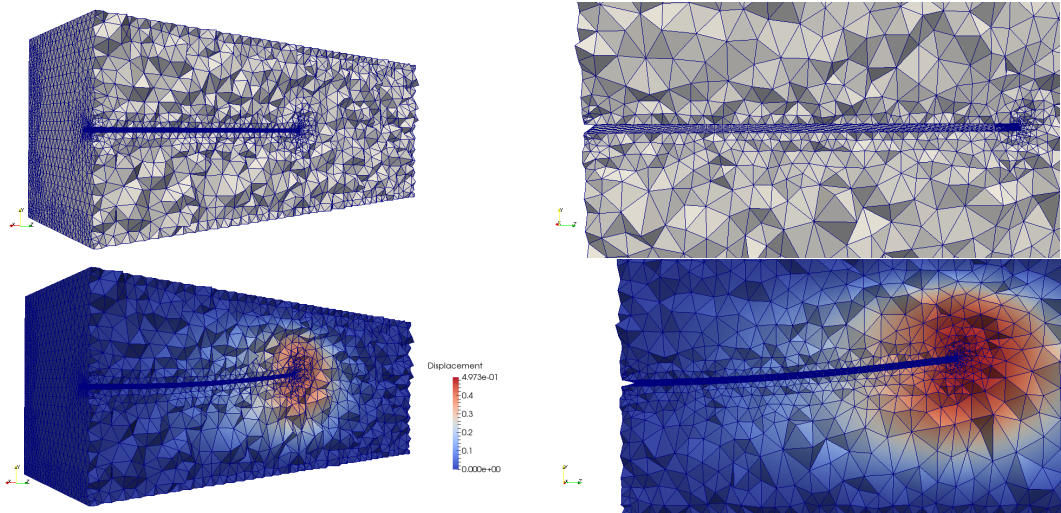
Figure 9: Fluid mesh motion around a wing: rest (top) and deformed (bottom) configuration; 3D (left) and section (right) view.

wind tunnel dimensions	$10 \times 5 \times 4\pi \ [\mathrm{m}^3]$
wing longitudinal dimension	$2\pi \ [\mathrm{m}]$
wing chord length	$1.01 \ [\mathrm{m}]$
# elements	169598
# nodes	36036
# internal nodes	21910
# boundary nodes	14126

Table 3: Fluid mesh motion around a wing: main properties of Ω_r and of Ω_h.

after 83.09 [s].

In order to reduce the computational costs, we resort to the ESIDW interpolation, by enriching the selection of control points in $\widehat{\mathcal{C}}$ with all the nodes on the left and right edge profiles as well as along the horizontal edges of the NACA profile (we refer to the previous test case for a motivation to this choice). Different values of radius R are selected for the faces of the (outer) box and for the sides of the (inner) wing. In particular, with similar considerations as in the previous section, we choose: $R_{top,b} = R_{bottom,b} = R_{front,b} = R_{rear,b} = 0.25$ [m] and $R_{right,b} = R_{left,b} = 0.125$ [m] for the box; $R_{top,w} = R_{bottom,w} = R_{right,w} = 0.025$ [m] for the wing. Parameters a and b are set to 0.8 and 1.3, respectively. **Algorithm 2** provides a subset $\widehat{\mathcal{C}}$ consisting of 9339 control points (see the enlarged view in Figure 10, bottom), so that matrix $\widehat{W}$ in (6) is now in $\mathbb{R}^{21910 \times 9339}$. As shown in the figure, control points are essentially located on the structure profile only.

The selection process reduces the computational time to 57.07 [s], and further reduction is possible taking a larger value of R as discussed below.

Finally, the $L^2(\Omega_h)$-norm of the relative error between the ESIDW and the IDW deformation is approximately 5.86%.

Sensitivity to R. We numerically check the sensitivity of IDW and ESIDW techniques to the selection radius, by mimicking the investigation in the previous section. For this purpose, we choose $R_{top,b} = R_{bottom,b} = R_{front,b} = R_{rear,b} = R$, $R_{right,b} = R_{left,b} = 0.5R$ for the box, and $R_{top,w} = R_{bottom,w} = R_{right,w} = 0.1R$ for the wing, while preserving the values previously adopted for a and b.

The trend exhibited by the number of control points in Figure 11, left is completely different with respect to the one in Figure 5, left. The cardinality of $\widehat{\mathcal{C}}$ is essentially the same as for the IDW approach until R sufficiently increases. Then, for $R > 0.1$, the cardinality reduces more
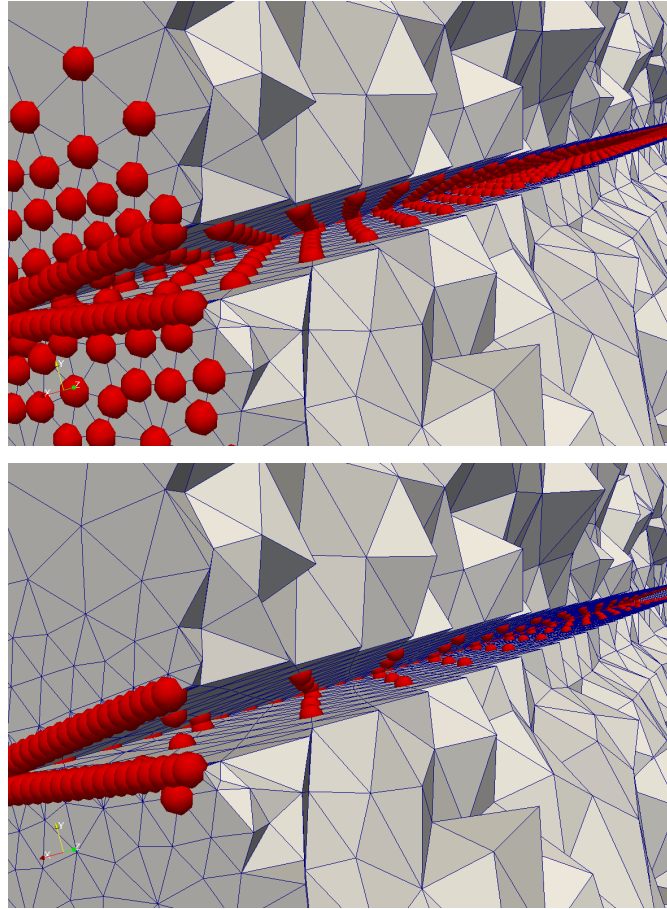
15

Figure 10: Fluid mesh motion around a wing: control point distribution associated with the IDW (top) and ESIDW (bottom) interpolation in correspondence with the clamped side.

mesh dimension	$50 \times 25 \times 10$ [m³]
hull length	2.5 [m]
# elements	30265
# nodes	7186
# internal nodes	3322
# boundary nodes	3864

Table 4: Fluid mesh motion around a rotating hull: main properties of Ω_r and of Ω_h.

and more ensuring, for instance, a gain of one order of magnitude for $R > 2$.

The central panel in Figure 11 computes the associated CPU time (in seconds), where now we have quantified the assembly and the deformation time, altogether. As expected, the trend of the computational time follows the one of the control point cardinality, as well as the $L^2(\Omega_h)$-norm of the relative error between ESIDW and IDW deformation, as shown in Figure 11, right. In contrast to Figure 6, left no stagnation of the error is detected when varying R.

Finally, concerning the quality characterizing the meshes yielded by IDW and ESIDW procedures, we have that the maximum and the mean value of $\mathcal{Q}$, independently of the adopted interpolation, is equal to 4.31 and 1.48, respectively with negligible variations (on the second decimal digit only) for ESIDW, as long as $R \leq 1$.
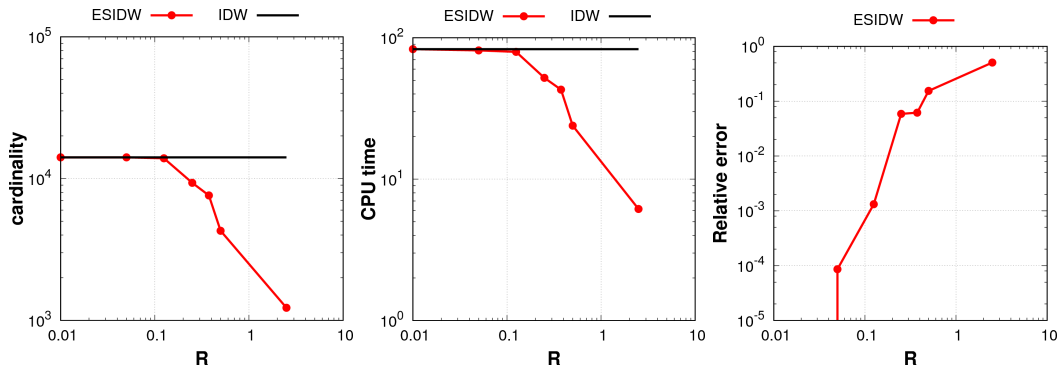

Figure 11: Fluid mesh motion around a wing: cardinality of the control point set (left), total CPU time (center), and the relative error (right) as a function of R.

2.3.3   Fluid mesh motion around a rotating hull

We conclude this section by testing the performances of the ESIDW interpolation when dealing with a FSI setting where a large deformation occurs. In more detail, we model a fluid mesh motion which results from the rotation of a structural domain in a naval engineering context. The initial configuration coincides with an outer box containing an inner Wigley hull [51] (see Figure 12, top). A rotation of $-5°$ with respect to the z-axis is successively applied. We refer to Table 4 for a summary of the main properties of the physical domain and of the corresponding discretization.

The standard IDW approach results in solving the linear system (3), matrix W being in $\mathbb{R}^{3322 \times 3864}$. This leads to a CPU time of 4.51 [s].

To reduce the computational burden, we apply **Algorithm 2**. The selection is performed by considering a radius $R = 1.5$ [m], $a = 0.8$ and $b = 1.3$. Notice that the value of R is comparable with the hull length. This allows a considerable reduction in the number of control points along the boundaries of the fluid domain. Moreover, to ensure that interior mesh nodes accurately capture the rotation of the hull, we switch on the enriching step (ii) of the selection procedure, by adding to $\widehat{\mathcal{C}}$ all the nodes belonging to the edge of the hull. The resulting distribution of control points is shown in Figure 12, top. Most of the points are identified by the constraint step, while very few nodes (only two in the specific case) are retained by the selection at step (i). As a result, the hull turns out to be sharply described by the control points. ESIDW
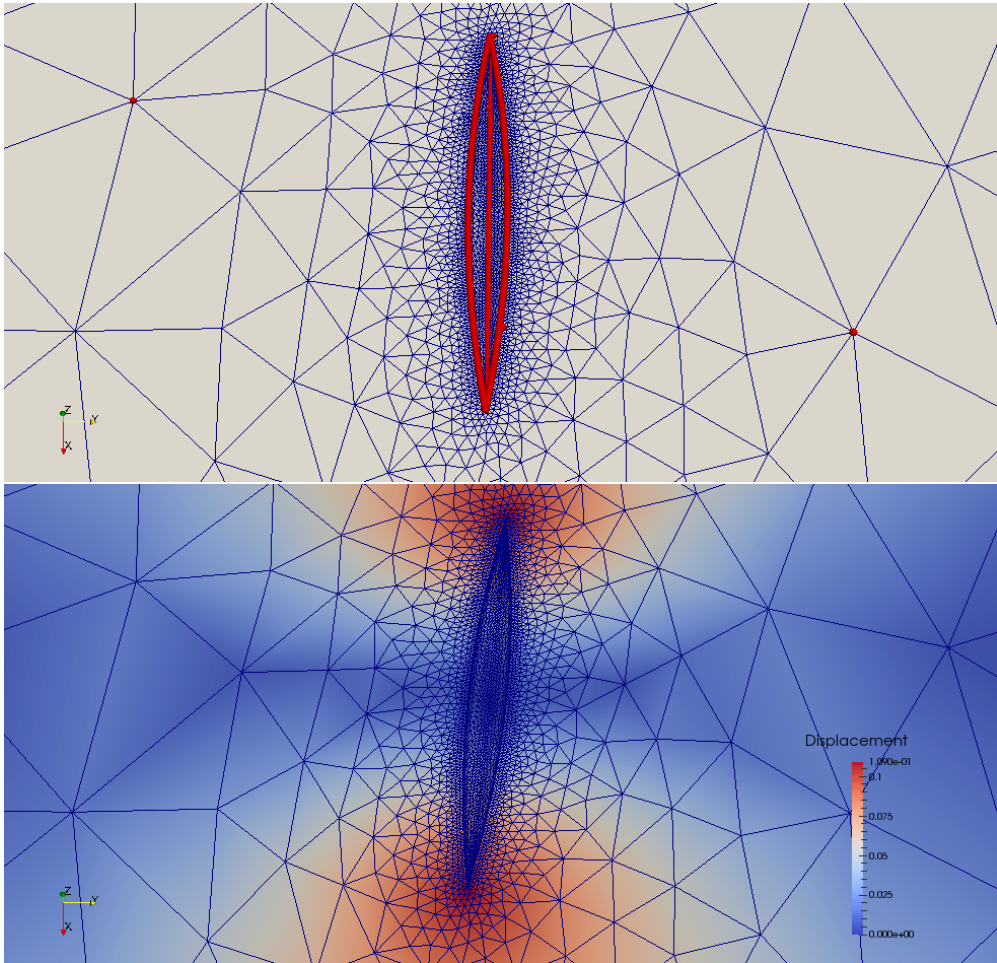
17

Figure 12: Fluid mesh motion around a rotating hull: control points (top) and deformed configuration (bottom) provided by the ESIDW interpolation.
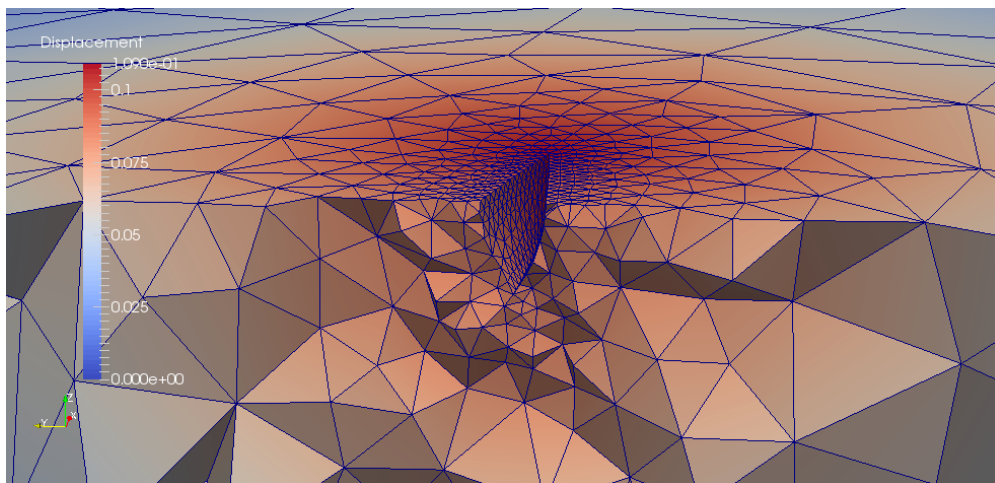

Figure 13: Fluid mesh motion around a rotating hull: detail of the deformed configuration provided by ESIDW interpolation.

procedure essentially halves the computational time, the CPU time of the deformation phase being now equal to 2.56 [s]. Figure 12, bottom displays the deformed fluid mesh, obtained by solving system (6), with $\widehat{W} \in \mathbb{R}^{3322 \times 1057}$. We also refer to Figure 13 for a detail of the deformed grid.

The computational cost reduction provided by ESIDW does not compromise the accuracy of the approximation. Indeed, the $L^2(\Omega_h)$-norm of the relative error between the ESIDW and the IDW deformation is 2.42%.

We have investigated the sensitivity to R also for this configuration, by mimicking the analysis in the previous section. Figure 14 provides the same results as in Figure 11. In contrast to this last case, we remark a less significant reduction in the number of the control points and of the total CPU time. Moreover, while for the wing configuration the ESIDW interpolation allows to gain six orders of magnitude in terms of accuracy for a sufficiently small R, only 2 orders less are obtained for the rotating hull configuration.

Finally, the rotation causes a slight increment in the maximum mesh quality (which changes from 2.47 in the reference configuration to 2.56 for the deformed one), while essentially preserving the mean value of $\mathcal{Q}$ (varying from 1.62 to 1.63 before and after the deformation). These values are essentially independent of the adopted interpolation and of R.
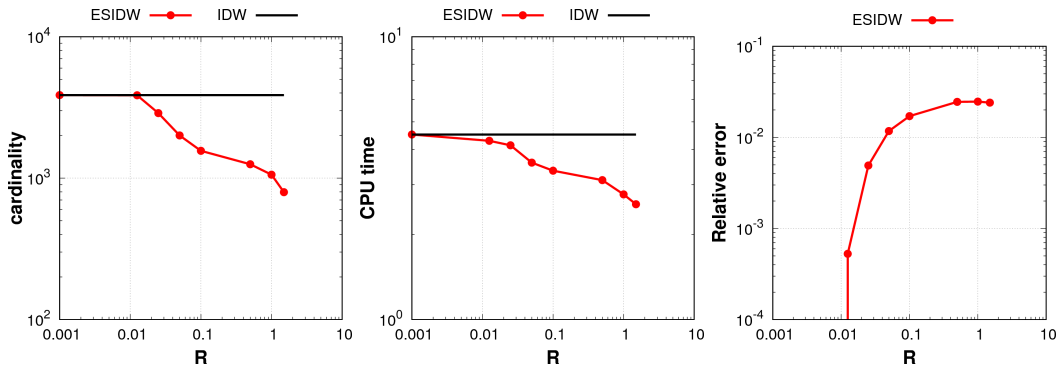

Figure 14: Fluid mesh motion around a rotating hull: cardinality of the control point set (left), total CPU time (center), and the relative error (right) as a function of R.

3   POD for SIDW shape morphing

We merge now the SIDW techniques presented in the previous section with a dimensionality reduction technique, following an offline-online paradigm [27]. The reduced basis will be determined via a *Proper Orthogonal Decomposition* (POD) technique (see, e.g., [27, 14, 49, 11]). POD reduces the dimensionality of a system by transforming the original variables into a new set of uncorrelated variables (called POD modes, or principal components), so that, ideally, the first few modes retain most of the 'energy' of the original system.

Generalizing notation, let $\boldsymbol{\mu} \in \mathbb{D}$ denote the generic parameter identifying the displacement $\mathbf{d}_{\widehat{c}}(\boldsymbol{\mu})$ of the control points $\widehat{\mathbf{c}}_k$ in $\widehat{\mathcal{C}}$. As in the test cases of the previous section, we assume $\mathbf{d}_{\widehat{c}}(\boldsymbol{\mu})$ to be an input for the shape morphing process. More in general, the map $\mathbf{d}_{\widehat{c}}(\boldsymbol{\mu})$ can be analytically provided (as in our synthetic test cases) or can be the output of a solver. For instance, when dealing with FSI problems, $\mathbf{d}_{\widehat{c}}(\boldsymbol{\mu})$ coincides with the evaluation of the structural displacements (computed by solving the elastodynamic equations) on the selected control points $\widehat{\mathcal{C}}$ along the fluid-structure interface.

According to (6), the deformation of the internal nodes $\mathbf{x}_j$, for $j = 1, \ldots, \mathcal{N}_h^i$, of the discretized reference domain Ω_h can be computed as

$$\mathbf{d}^i(\boldsymbol{\mu}) = \widehat{W}\mathbf{d}_{\widehat{c}}(\boldsymbol{\mu}), \qquad (8)$$

the dependence on the parameter being highlighted. Notice that, while both the input displacement $\mathbf{d}_{\widehat{c}}(\boldsymbol{\mu})$ and the output deformation $\mathbf{d}^i(\boldsymbol{\mu})$ depend on $\boldsymbol{\mu}$, the SIDW matrix $\widehat{W}$ is parameter independent.

19

During the POD offline stage, we consider a training set, $\Xi_{\text{train}} = \{\boldsymbol{\mu}_n\}_{n=1}^{n_{\text{train}}}$, of n_{train} values for the parameter $\boldsymbol{\mu}$. With each parameter $\boldsymbol{\mu}_n$, we associate a certain displacement $\mathbf{d}_{\widehat{c}}(\boldsymbol{\mu}_n)$ of $\widehat{\mathcal{C}}$, and we compute the corresponding deformation $\mathbf{d}^i(\boldsymbol{\mu}_n)$ in (8). This allows us to assemble the so-called *snapshot* matrix

$$\mathcal{U} = [\mathbf{d}^i(\boldsymbol{\mu}_1), \cdots, \mathbf{d}^i(\boldsymbol{\mu}_{n_{\text{train}}})] \in \mathbb{R}^{\mathcal{N}_h^i \times n_{\text{train}}}, \tag{9}$$

whose columns store the different scenarios induced by the training set of deformations. To extract the desired reduced basis, we perform now the Singular Value Decomposition (SVD) of matrix $\mathcal{U}$, so that

$$\mathcal{U} = \mathcal{W}\Sigma\mathcal{V}^T, \tag{10}$$

where

$$\mathcal{W} = [\boldsymbol{\zeta}_1, \boldsymbol{\zeta}_2, \cdots, \boldsymbol{\zeta}_{\mathcal{N}_h^i}] \in \mathbb{R}^{\mathcal{N}_h^i \times \mathcal{N}_h^i}$$

and

$$\mathcal{V} = [\boldsymbol{\Psi}_1, \boldsymbol{\Psi}_2, \cdots, \boldsymbol{\Psi}_{n_{\text{train}}}] \in \mathbb{R}^{n_{\text{train}} \times n_{\text{train}}}$$

are the orthogonal matrices of the *left* and of the *right singular vectors* of $\mathcal{U}$, while $\Sigma \in \mathbb{R}^{\mathcal{N}_h^i \times n_{\text{train}}}$ is a rectangular matrix of the same size as $\mathcal{U}$, whose only non-zero entries are the positive real diagonal entries, $\sigma_1 \geq \sigma_2 \geq \cdots \geq \sigma_r > 0$, which represent the *singular* (or *principal*) values of $\mathcal{U}$, $r \leq n_{\text{train}}$ being the rank of $\mathcal{U}$ [25].

The reduced *POD basis* is thus identified by a subset of the left singular vectors of $\mathcal{U}$ collected in the *POD basis matrix*

$$\mathcal{Z} = [\boldsymbol{\zeta}_1, \cdots, \boldsymbol{\zeta}_N] \in \mathbb{R}^{\mathcal{N}_h^i \times N}. \tag{11}$$

with $N \leq r$. The integer N can be selected via different criteria. In particular, since the energy contained in the discarded (i.e., the last $r - N$) POD modes is provided by

$$E_{\mathcal{U}}(N) = \frac{\sum_{n=N+1}^r \sigma_n^2}{\sum_{i=1}^r \sigma_n^2}, \tag{12}$$

we set a tolerance ε and choose N as the first integer such that $E_{\mathcal{U}}(N) \leq \varepsilon$. The identification of the POD basis concludes the offline phase.

The online phase starts from the choice of a new value $\boldsymbol{\mu}^* \in \mathbb{D}$ for the parameter, i.e., with the assignment of a new displacement $\mathbf{d}_{\widehat{c}}(\boldsymbol{\mu}^*)$ to the control points in $\widehat{\mathcal{C}}$. The POD basis is then exploited to approximate the corresponding deformation $\mathbf{d}^i(\boldsymbol{\mu}^*)$ of the internal nodes in Ω_h, defined as

$$\mathbf{d}^i(\boldsymbol{\mu}^*) = \widehat{W}\mathbf{d}_{\widehat{c}}(\boldsymbol{\mu}^*). \tag{13}$$

In particular, we look for a suitable linear combination of the POD basis functions $\{\boldsymbol{\zeta}_l\}_{l=1}^N$, such that

$$\mathcal{Z}\,\boldsymbol{\beta}(\boldsymbol{\mu}^*) = \widehat{W}\mathbf{d}_{\widehat{c}}(\boldsymbol{\mu}^*) \tag{14}$$

and where $\boldsymbol{\beta}(\boldsymbol{\mu}^*) \in \mathbb{R}^N$, with $[\boldsymbol{\beta}(\boldsymbol{\mu}^*)]_l = \beta_l$ and $l = 1, \ldots, N$, is a vector of unknown coefficients depending on parameter $\boldsymbol{\mu}^*$. We manipulate (14) as

$$\widehat{W}^+\mathcal{Z}\,\boldsymbol{\beta}(\boldsymbol{\mu}^*) = \mathbf{d}_{\widehat{c}}(\boldsymbol{\mu}^*) \tag{15}$$

where $\widehat{W}^+ \in \mathbb{R}^{\mathcal{N}_{\widehat{c}} \times \mathcal{N}_h^i}$ denotes the pseudo-inverse of $\widehat{W}$ [25]. The vector $\boldsymbol{\beta}(\boldsymbol{\mu}^*)$ is then computed in the least squares sense, i.e., by solving the normal equation system

$$\mathcal{Z}^T(\widehat{W}^+)^T\,\widehat{W}^+\mathcal{Z}\,\boldsymbol{\beta}(\boldsymbol{\mu}^*) = \mathcal{Z}^T(\widehat{W}^+)^T\mathbf{d}_{\widehat{c}}(\boldsymbol{\mu}^*), \tag{16}$$

assuming that $\widehat{W}^+\mathcal{Z}$ has full column rank.

The system we are lead to solve has size N, being $\mathcal{Z}^T(\widehat{W}^+)^T\,\widehat{W}^+\mathcal{Z} \in \mathbb{R}^{N \times N}$ and $\mathcal{Z}^T(\widehat{W}^+)^T \in \mathbb{R}^{N \times \mathcal{N}_{\widehat{c}}}$. The deformation of the domain is finally computed via the product in (13).

Remark 1. As alternative to system (16), one can derive from (14)

$$\boldsymbol{\beta}(\boldsymbol{\mu}^*) = \mathcal{Z}^+ \widehat{W} \mathbf{d}_{\widehat{c}}(\boldsymbol{\mu}^*), \tag{17}$$

i.e., solve the normal equation system

$$\mathcal{Z}^T \mathcal{Z}\, \boldsymbol{\beta}(\boldsymbol{\mu}^*) = \mathcal{Z}^T \widehat{W} \mathbf{d}_{\widehat{c}}(\boldsymbol{\mu}^*),$$

assuming $\mathcal{Z}$ to have full column rank.

A comparison between this approach and the one proposed above is beyond the scope of this work. Nevertheless, we remark that the term $(\widehat{W}^+)^T \widehat{W}^+$ in (16) can be conceived as a weighting factor which takes into account the mesh connectivity.

Indeed, (17) results from the solution of the minimization problem

$$\mathcal{Z}\boldsymbol{\beta}(\boldsymbol{\mu}^*) = \underset{\mathbf{x}\in\mathrm{range}(\mathcal{Z})}{\mathrm{argmin}}\ \|\mathbf{x} - \widehat{W}\mathbf{d}_{\widehat{c}}(\boldsymbol{\mu}^*)\|_2,$$

while (16) stems from the minimization problem

$$\mathcal{Z}\boldsymbol{\beta}(\boldsymbol{\mu}^*) = \underset{\mathbf{x}\in\mathrm{range}(\mathcal{Z})}{\mathrm{argmin}}\ \|\mathbf{x} - \widehat{W}\mathbf{d}_{\widehat{c}}(\boldsymbol{\mu}^*)\|_w,$$

where the weighted norm $\|\cdot\|_w$ is defined as

$$\|\mathbf{x}\|_w = \sqrt{\mathbf{x}^T (\widehat{W}^+)^T\, \widehat{W}^+ \mathbf{x}}.$$

We note that the withed approach in (16) entails stronger assumptions compared with (17). In particular, problem (17) only requires $\mathcal{Z}$ to be full rank, while (16) necessitates $\widehat{W}^+\mathcal{Z}$ to be full rank. As a result, condition $\mathcal{N}_{\widehat{c}} \geq N$ has to be added for the weighted approach, while such a condition is not required for the other approach. In practice, we stress that condition $\mathcal{N}_{\widehat{c}} \geq N$ is trivially verified since we are interested in performing a dimensionality reduction.

We observe that both the matrices in (16) can be computed once and for all at the end of the offline stage. Thus, the online phase reduces to evaluate the matrix-vector product on the right-hand side of (16), to solve a linear system of size N and then to compute the linear combination $\mathcal{Z}\,\boldsymbol{\beta}(\boldsymbol{\mu}^*)$. In terms of computational burden, the most effort involves the internal nodes. In more detail, we are comparing the full problem (13) demanding $O(\mathcal{N}_h^i \cdot \mathcal{N}_{\widehat{c}})$ floating point operations with the POD approach characterized by $O(N^3 + N \cdot \mathcal{N}_{\widehat{c}} + \mathcal{N}_h^i \cdot N)$ operations. This suggests that, if $N \ll \mathcal{N}_{\widehat{c}}$, we expect a computational saving via the reduced approach. This will be numerically verified in the next section.

The complete POD-SIDW interpolation procedure is itemized in **Algorithm 3** when applied to a generic shape morphing context. The POD-ESIDW variant can be set in a straightforward way simply by switching on the optional step (ii) of **Algorithm 2** at the first item of the offline phase. With a view to a FSI problem, the same setting as for **Algorithm 2** is adopted.

3.1   POD-SIDW algorithms in action

We come back to the test cases in Section 2.3 to investigate possible benefits on SIDW interpolation techniques due to POD. In particular, we quantify the computational improvements in terms of CPU time and accuracy of the approximation.

3.1.1   Structural deformation of a wing

We apply the POD reduction procedure to a parameter dependent variant of the configuration in Section 2.3.1. To this aim, we impose the parametrized vertical displacement

$$\delta y = \delta y(z; \mu) = \mu z^2 \tag{18}$$

to the wing, where the parameter μ is a scalar varying in the interval $\mathbb{D} = [0, 1.3]$.

We focus on the standard IDW and on the ESIDW interpolation techniques. With reference to the ESIDW approach, we preserve the two different choices done for the selection radius in

Algorithm 3 POD-SIDW interpolation for shape morphing

OFFLINE PHASE:

(a) apply the SELECTION PHASE of **Algorithm 2** to extract $\widehat{\mathcal{C}}$ and to assemble the SIDW matrix $\widehat{W}$;

(b) **for each** $\boldsymbol{\mu}_n \in \Xi_{\mathbf{train}}$

apply the DEFORMATION PHASE of **Algorithm 2** to compute $\mathbf{d}^i(\boldsymbol{\mu}_n)$ via (8);

end for

(c) assemble the snapshot matrix $\mathcal{U}$ in (9);

(d) extract the POD basis matrix $\mathcal{Z}$ in (11);

(e) compute matrices $\mathcal{Z}^T(\widehat{W}^+)^T \widehat{W}^+ \mathcal{Z}$ and $\mathcal{Z}^T(\widehat{W}^+)^T$ in (16).

ONLINE PHASE: chosen $\boldsymbol{\mu}^* \in \mathbb{D}$:

(f) solve system (16) to derive the weights in $\boldsymbol{\beta}(\boldsymbol{\mu}^*)$;

(g) compute the linear combination $\mathcal{Z}\,\boldsymbol{\beta}(\boldsymbol{\mu}^*)$.

---

method	card($\widehat{\mathcal{C}}$)	CPU time(OFFLINE)	card($\mathcal{Z}$)	CPU time(ONLINE)	Error
IDW	1666	-	-	0.25 [s]	-
ESIDW	390	-	-	0.034 [s]	1.06 %
POD-IDW	1666	90.93 [s]	1	0.013 [s]	negligible
POD-ESIDW	390	76.84 [s]	1	0.013 [s]	1.10 %

Table 5: Structural deformation of a wing: comparison between the basic IDW and ESIDW techniques and the corresponding POD variants.

Section 2.3.1, by picking $R = R_{lr} = 0.05$ [m] and $R = R_{tb} = 0.5$ [m] for the left and right and for the top and bottom surfaces of the wing, respectively. Then, accordingly to Section 2.3.1, the enrichment is performed by adding in $\widehat{\mathcal{C}}$ all the nodes along the left, the right and the horizontal edges of the NACA profile.

To build the snapshot matrix $\mathcal{U}$, we randomly select $n_{\mathrm{train}} = 100$ values in $\mathbb{D}$ which identify the set Ξ_{train}. Then, to extract the POD basis we fix $\varepsilon = 10^{-5}$ as tolerance on the energy $E_{\mathcal{U}}(N)$ in (12). Finally, we choose $\mu^* = 0.65$ as parameter value during the online phase.

Table 5 compares the performances of the plain IDW and ESIDW interpolations with the corresponding POD variants. The second column provides the number of control points employed for morphing the original structure, being understood that $\widehat{\mathcal{C}} \equiv \mathcal{C}$ when dealing with the IDW approach. The third column gathers the CPU time required by the offline phase of **Algorithm 3** to construct the response matrix, to extract the POD basis, whose cardinality is furnished in the fourth column, and to assemble matrices $\mathcal{Z}^T(\widehat{W}^+)^T \widehat{W}^+ \mathcal{Z}$ and $\mathcal{Z}^T(\widehat{W}^+)^T$ in (16). The fifth column summarizes the CPU time required to perform the shape morphing via (3) and (6) in the case of the basic IDW and SIDW interpolations, respectively; for the POD variants, this coincides with the CPU time demanded by the online phase, i.e., by the resolution of system (16) and by the computation of the linear combination $\mathcal{Z}\boldsymbol{\beta}(\boldsymbol{\mu}^*)$. Finally, the last column investigates the accuracy of the provided deformation by collecting the value of the $L^2(\Omega_h)$-norm of the relative error between the computationally cheaper deformations and the reference IDW shape.

Concerning the specific values in Table 5, we observe that both the POD variants identify a minimal reduced basis, a single POD mode being sufficient to ensure the desired tolerance. Figure 15, left shows the decay of the spectrum, normalized to the maximum singular value, for both the POD-IDW and the POD-ESIDW reduction. The first approach exhibits a more evident drop so that a single mode ensures actually an accuracy of 10^{-7} (considerably higher than the one demanded). The POD-ESIDW procedure in this case requires a larger number of modes to guarantee the same accuracy, for instance, two modes are demanded for $\varepsilon = 10^{-6}$ whereas four modes are required for $\varepsilon = 10^{-7}$. The computational time demanded by the offline phase of both the POD-IDW and POD-ESIDW procedures is not negligible, being equal to 90.93 [s] and to 76.84 [s], respectively. Nevertheless, this phase takes place just once and, as expected, allows a considerable saving in the actual computation of the shape morphing (0.013 [s] to be compared with 0.25 [s] and with 0.034 [s], respectively), thus becoming the ideal tool, for instance, for a
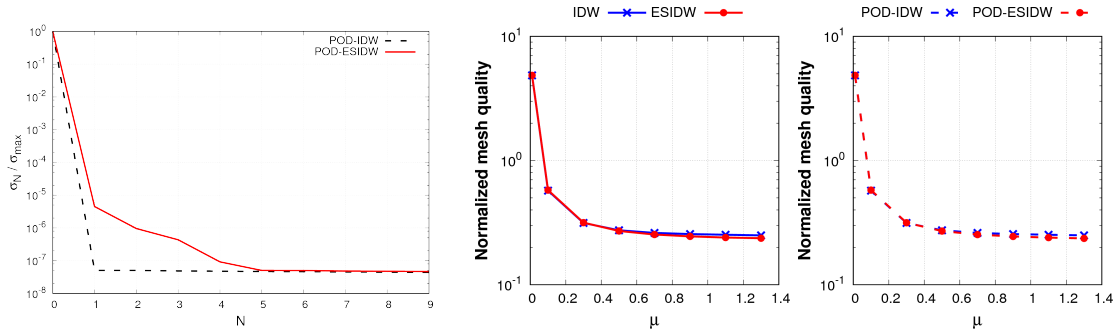
Figure 15: Structural deformation of a wing: spectrum decay (of the first ten singular values) for POD-IDW and POD-ESIDW procedures (left); comparison in terms of mesh quality between IDW and ESIDW interpolation (center) and POD-IDW and POD-ESIDW reduction (right) in the presence of large deformations.

method	card($\widehat{\mathcal{C}}$)	CPU time(OFFLINE)	card($\mathcal{Z}$)	CPU time(ONLINE)	Error
IDW	14126	-	-	83.09 [s]	-
ESIDW	9339	-	-	57.07 [s]	5.86%
POD-IDW	14126	2479.51 [s]	1	0.55 [s]	negligible
POD-ESIDW	9339	1613.65 [s]	1	0.55 [s]	5.94 %

Table 6: Fluid mesh motion around a wing: comparison between the basic IDW and ESIDW techniques and the corresponding POD variants.

multi-query context. Moreover, the POD procedure does not compromise the accuracy of the approximation, the error (with respect to standard IDW interpolation) being negligible (less than 10^{-8}) in the POD-IDW case, while increasing from 1.06% to 1.10% when dealing with the enriched procedure.

Finally, we check how the POD procedure does influence the quality of the deformed mesh, with emphasis on large deformations. In particular, since the mesh quality is expected to deteriorate for larger and larger displacements (of magnitude up to $1.3 \cdot (2\pi)^2$, i.e. more than 800% of the longitudinal dimension 2π), we consider a normalized mesh quality index, defined as the ratio between the mean mesh quality and the maximum displacement measured at the side of the wing which is not clamped. A cross comparison of the plots in Figure 15, center and right, shows that the POD approach essentially has no influence on the mesh quality as well as the ESIDW interpolation, the selected index preserving a constant value of about 0.28 for $\mu > 0.3$.

3.1.2 Fluid mesh motion around a wing

We move to the parametric version of the FSI test case in Section 2.3.2, dealing with the fluid mesh motion around a NACA0012 profile. The wing is now deformed by the parametrized vertical displacement (18), with $\mu \in \mathbb{R}$ varying in $\mathbb{D} = [0, 0.05]$.

We compare POD-IDW with POD-ESIDW and with the corresponding procedures without any dimensionality reduction. The parameters R, a and b characterizing the selection procedure are the same as in Section 2.3.2, as well as the constraints driving the enrichment step of **Algorithm 2**. The training set Ξ_{train} is now constituted of 20 samples randomly distributed in $\mathbb{D}$, and the tolerance ε employed in the POD offline phase is set to 10^{-5} as in the previous test case. The actual deformation is then identified by $\mu^* = 0.01$.

Table 6 offers a summary of the performances of the proposed methods. The successive columns collect the same quantities as in Table 5. The advantages due to the enriched selective procedure have been already highlighted in Section 2.3.2, both in terms of reduction of the control points and of the CPU time.

A further saving in the computational time demanded for the actual structure deformation is obtained via POD, the online CPU time reducing to 0.55 [s] for both the POD-IDW and the POD-ESIDW procedures. The global CPU time reduction due to a selection of the control points

method	card($\widehat{\mathcal{C}}$)	CPU time(OFFLINE)	card($\mathcal{Z}$)	CPU time(ONLINE)	Error
IDW	3864	-	-	4.51 [s]	-
ESIDW	1057	-	-	2.56 [s]	2.42%
POD-IDW	3864	203.07 [s]	1	0.38 [s]	0.23% ∼ 2.85%
			2	0.38 [s]	negligible
POD-ESIDW	1057	150.26 [s]	1	0.38 [s]	2.62% ∼ 3.84%
			2	0.38 [s]	2.43%

Table 7: Fluid mesh motion around a rotating hull: comparison between the basic IDW and ESIDW techniques and the corresponding POD variants.

combined with a POD procedure is of two orders of magnitude with respect to the standard IDW approach, for each new morphing. This considerable saving is justified by the small dimension of the POD basis, consisting of a unique mode (notice that, for this test case, the trend of the first ten singular values associated with the two POD procedures is exactly the same, as Figure 16, left shows). The POD offline phase remains the most time consuming part of the whole procedure, requiring 2479.51 [s] and 1613.65 [s] in the POD-IDW and POD-ESIDW case, respectively.
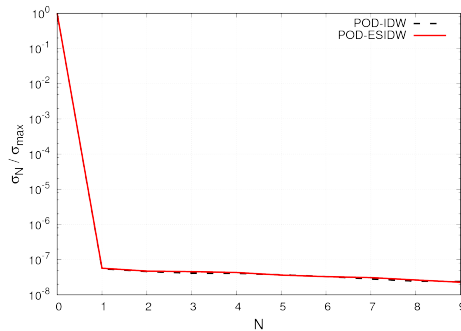

Figure 16: Fluid mesh motion around a wing: spectrum decay (for the first ten singular values) for POD-IDW and POD-ESIDW procedures.

Finally, we remark that the accuracy of the POD-ESIDW interpolation is essentially limited by the selection applied to control points. Indeed, the POD-ESIDW approach entails a relative error of 5.94% to be compared with an error of 5.86% for the basic ESIDW method.

3.1.3 Fluid mesh motion around a rotating hull

We conclude the numerical assessment by studying the benefits provided by the POD reduction onto the large deformation setting in Section 2.3.3. The rotation of the hull with respect to the z axis is now parametrized, μ coinciding with the rotation angle assuming values in the range $\mathbb{D} = [-36°, \ 0°]$.

As in the two previous sections, POD is combined with IDW and ESIDW interpolations. For the control point selection procedure, we adopt the same values for R, a and b as in Section 2.3.3. To build the snapshot matrix and to extract the POD basis, we exploit $n_{\text{train}} = 50$ values for parameter μ, randomly distributed in $\mathbb{D}$. The tolerance ε for the energy check is set to 10^{-5}. Finally, the target configuration is identified by the parameter $\mu^* = -5°$. From Figure 17, left, we realize that few POD modes suffice to describe the new rotation with a good accuracy. In particular, tolerance ε is reached by resorting only to two modes.

The performances of POD-IDW and POD-ESIDW methods are summarized in Table 7, whose columns are organized as in Tables 5 and 6. The computational gain yielded by ESIDW with respect to the standard IDW interpolation is evident, following the analysis in Section 2.3.3. Concerning the combined effect of selecting the control points and resorting to a POD reduction, Table 7 quantitatively confirms what already remarked for the two previous test cases. In particular, while ESIDW manages almost to halve the CPU time required for a shape morphing

24

compared to the standard IDW approach, a successive reduction of about one seventh is reached via POD, two basis functions being enough to reach the prescribed tolerance ε. Similar conclusions hold when comparing IDW with POD-IDW, the CPU time being reduced of about eleven times when resorting to a POD space constituted of two basis functions only. The price to pay for this computationally cheap shape morphing is represented, according to an offline/online paradigm, by the offline phase in **Algorithm 3**, which demands 203.07 [s] and 150.26 [s] for the POD-IDW and the POD-ESIDW approach, respectively.

Figure 17, center compares the trend of the $L^2(\Omega_h)$-norm of the relative error between the POD-IDW (POD-ESIDW) and the standard IDW deformation as a function of the rotation angle, when either one or two POD modes are adopted to predict the new deformation. The plot of the POD-IDW procedure associated with two POD modes is omitted, the corresponding relative error being essentially negligible (less than 10^{-8}). The accuracy guaranteed by the POD-IDW approach strongly depends on the selected angle when a single POD mode is employed, with a significant improvement in the presence of large rotations. On the contrary, a low sensitivity to the rotation angle is exhibited by the POD-ESIDW reduction, the error always being of the order of 10^{-2}. Moreover, from the last column in Table 7, we deduce that the control point selection still represents the principal responsible for an accuracy deterioration regardless of the selected angle, the relative error remaining essentially the same when combining the ESIDW approach with a POD reduction.

Finally, as shown in Figure 17, right, the POD reduction does not perturb essentially the quality of the deformed mesh with respect to the standard ESIDW approach, and exhibits a contained dependence on the applied rotation.
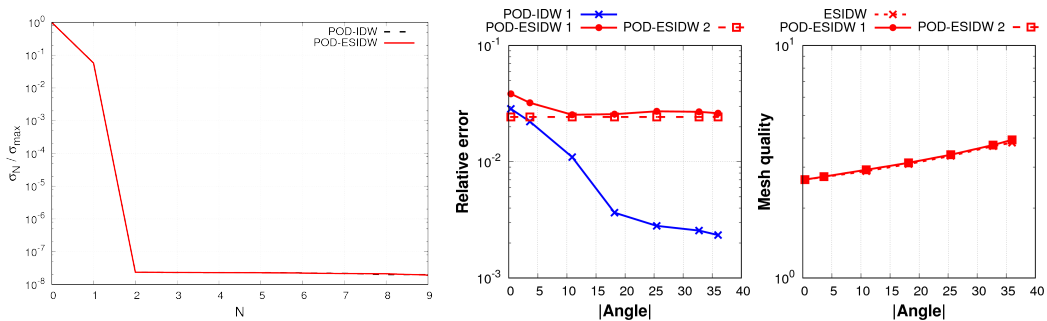

Figure 17: Fluid mesh motion around a rotating hull: spectrum decay (for the first ten singular values) for POD-IDW and POD-ESIDW procedures; relative error as a function of the rotation angle for POD-IDW and POD-ESIDW reductions (center); comparison in terms of mesh quality between ESIDW and POD-ESIDW procedures (right).

4 Conclusions and perspectives

We have proposed two strategies (and a possible combination of these) to reduce the dimensionality of shape morphing techniques based on IDW. The first approach (the SIDW/ESIDW interpolation), based on a geometric selection of the control points, is very general and can be applied to any dimension and to arbitrary meshes. SIDW/ESIDW variants, tested on configurations of interest in engineering applications, such as airfoils and hulls, proved to be very effective since they considerably reduce the set of control points (i.e., the CPU time) without excessively compromising the accuracy of the approximation.

A further reduction of the computational burden is then carried out by means of a POD (offline phase) and a least squares regression (online phase) techniques. This allows us to convert any shape morphing into the resolution of a linear system of size N, with N the number of selected POD basis functions. In the considered test cases, the number N turns out to be very small. Indeed, one or, at most, two POD basis functions were enough to guarantee a tolerance of 10^{-5} to the energy contained in the discarded POD modes. We have combined POD dimensionality reduction with IDW and ESIDW interpolations, event though any shape morphing algorithm can be alternatively considered.

The numerical verification in Section 3.1 shows that the combined POD-IDW and POD-ESIDW techniques lead to a large computational saving, up to two orders of magnitude on the CPU time. The offline phase remains the most time-consuming part of the procedure, according to an offline/online paradigm. Finally, an accuracy analysis highlights that SIDW/ESIDW entail very small relative errors (few percentage points) with respect to the standard IDW procedure, while POD reduction does not significantly contribute further.

A possible future development of this work might concern the integration of the proposed methods into a FSI solver, or the application to several optimization contexts. An adaptive selection of the control points driven by some quantity of interest, combination with reduction procedures for parametrized problems (e.g., [7, 16, 27]), as well as the use of active subspaces method [17, 47] as pre-processing, represent further topics of interest for the following of the current work.

Acknowledgments

References

[1] SALOME Platform. `http://www.salome-platform.org/`.

[2] J. Ahrens, B. Gavenci, and C. Law. *ParaView: An End-User Tool for Large Data Visualization, Visualization Handbook*. Elsevier, 2005.

[3] J. Anttonen, P. King, and P. Beran. POD-based reduced-order models with deforming grids. *Mathematical and Computer Modelling*, 38(1):41 – 62, 2003.

[4] F. Ballarin. *Reduced-Order Models for Patient-Specific Haemodynamics of Coronary Artery Bypass Grafts*. PhD thesis, , Department of Mathematics, Politecnico di Milano, , 2015. `http://hdl.handle.net/10589/102804`.

[5] F. Ballarin, E. Faggiano, S. Ippolito, A. Manzoni, A. Quarteroni, G. Rozza, and R. Scrofani. Fast simulations of patient-specific haemodynamics of coronary artery bypass grafts based on a POD–Galerkin method and a vascular shape parametrization. *Journal of Computational Physics*, 315:609–628, 2016.

[6] F. Ballarin, A. Manzoni, G. Rozza, and S. Salsa. Shape optimization by Free-Form Deformation: existence results and numerical solution for Stokes flows. *Journal of Scientific Computing*, 60(3):537–563, 2014.

[7] D. Baroli, C. Cova, S. Perotto, L. Sala, and A. Veneziani. Hi-POD solution of parametrized fluid dynamics problems: preliminary results. In P. Benner, M. Ohlberger, A. Patera, G. Rozza, and K. Urban, editors, *Model Reduction of Parametrized Systems*, volume 17 of *MS&A Series*, chapter 15, pages 235–254. Springer International Publishing, 2017.

[8] Y. Bazilevs, K. Takizawa, and T. Tezduyar. *Computational Fluid-Structure Interaction: Methods and Applications*. John Wiley & Sons, 2013.

[9] Y. Bazilevs, K. Takizawa, and T. Tezduyar. *Computational Fluid-Structure Interaction: Methods and Applications*. John Wiley & Sons, 2013.

[10] A. Beckert and H. Wendland. Multivariate interpolation for fluid-structure-interaction problems using Radial Basis Functions. *Aerospace Science and Technology*, 5:125–134, 2001.

[11] P. Benner, S. Gugercin, and K. Willcox. A survey of projection-based model reduction methods for parametric dynamical systems. *SIAM Review*, 57(4):483–531, 2015.

[12] M. Buhmann. *Radial Basis Functions*, volume 12 of *Cambridge Monographs on Applied and Computational Mathematics*. Cambridge University Press, UK, 2003.

[13] H.-J. Bungartz and M. Schäfer. *Fluid-Structure Interaction: Modelling, Simulation, Optimisation*, volume 53. Springer Science & Business Media, 2006.

[14] J. Burkardt, M. Gunzburger, and H.-C. Lee. POD and CVT-based reduced-order modeling of Navier–Stokes flows. *Computer Methods in Applied Mechanics and Engineering*, 196:337–355, 2006.

[15] J. Cebral and R. Lohner. Conservative load projection and tracking for fluid-structure problems. *AIAA Journal*, 35:687–692, 1997.

[16] F. Chinesta, R. Keunings, and A. Leygue. *The Proper Generalized Decomposition for Advanced Numerical Simulations: A Primer*. Springer, 2014. Springer Briefs in Applied Sciences and Technologies.

[17] P. Constantine. *Active Subspaces: Emerging Ideas for Dimension Reduction in Parameter Studies*. SIAM, 2015.

[18] A. Crivellaro, S. Perotto, and S. Zonca. Reconstruction of 3D scattered data via radial basis functions by efficient and robust techniques. *Applied Numerical Mathematics*, 113:93–108, 2017.

[19] S. Deparis, D. Forti, and A. Quarteroni. A rescaled localized radial basis function interpolation on non-Cartesian and non-conforming grids. *SIAM Journal on Scientific Computing*, 36(6), 2014.

[20] I. Dryden and K. Mardia. *Statistical Shape Analysis*. John Wiley and Sons, Chichester, 1998.

[21] C. Farhat, M. Lesoinne, and P. Le Tallec. Load and motion transfer algorithms for fluid/structure interaction problems with non-matching discrete interfaces: momentum and energy conservation, optimal discretization and application to aeroelasticity. *Computer Methods in Applied Mechanics and Engineering*, 157(1):95–114, 1998.

[22] D. Forti. Comparison of Shape Parametrization Techniques for Fluid-Structure Interaction Problems. Master's thesis, , Politecnico di Milano, Italy, , 2012.

[23] D. Forti and G. Rozza. Efficient geometrical parametrization techniques of interfaces for reduced-order modelling: application to fluid–structure interaction coupling problems. *International Journal of Computational Fluid Dynamics*, 28(3–4):158–169, 2014.

[24] P. Frey and P.-L. George. *Mesh Generation: Application to Finite Elements*. ISTE Ltd and John Wiley & Sons, Inc, 2nd edition, 2010.

[25] G. Golub and C. Van Loan. *Matrix Computation*. The Johns Hopkins University Press, Baltimore, Fourth edition, 2013.

[26] R. Guibert, K. McLeod, A. Caiazzo, T. Mansi, M. Fernández, M. Sermesant, X. Pennec, I. Vignon-Clementel, Y. Boudjemline, and J.-F. Gerbeau. Group-wise construction of reduced models for understanding and characterization of pulmonary blood flows from medical images. *Medical Image Analysis*, 18(1):63–82, 2014.

[27] J. Hesthaven, G. Rozza, and B. Stamm. *Certified Reduced Basis Methods for Parametrized Partial Differential Equations*. MS&A Series. Springer International Publishing, 2016.

[28] B. Kirk, J. Peterson, R. Stogner, and G. Carey. libMesh: a C++ library for parallel adaptive mesh refinement/coarsening simulations. *Engineering with Computers*, 22(3-4):237–254, 2006.

[29] H. Lamousin and W. Waggenspack. NURBS-based free-form deformations. *IEEE Comput. Graph. Appl.*, 14(6):59–65, 1994.

[30] T. Lassila and G. Rozza. Parametric free-form shape design with PDE models and reduced basis method. *Computer Methods in Applied Mechanics and Engineering*, 199(23–24):1583–1592, 2010.

[31] M. Lombardi. *Numerical Simulation of a Sailing Boat: Free Surface, Fluid-Structure Interaction and Shape Optimization*. PhD thesis, , Ecole Polyechnique Fédérale de Lausanne, , 2012.

[32] M. Lombardi, N. Parolini, A. Quarteroni, and G. Rozza. Numerical simulation of sailing boats: dynamics, FSI, and shape optimization. In A. Frediani and G. Buttazzo, editors, *Variational Analysis and Aerospace Engineering: Mathematical Challenges for Aerospace Design*, volume 66, pages 339–377. Springer US, 2012.

[33] G. Lu and D. Wong. An adaptive inverse-distance weighting spatial interpolation technique. *Computers & Geosciences*, 34:1044–1055, 2008.

[34] A. Manzoni, A. Quarteroni, and G. Rozza. Model reduction techniques for fast blood flow simulation in parametrized geometries. *International Journal for Numerical Methods in Biomedical Engineering*, 28(6–7):604–625, 2012.

[35] K. McLeod, A. Caiazzo, M. Fernández, T. Mansi, I. Vignon-Clementel, M. Sermesant, X. Pennec, Y. Boudjemline, and J.-F. Gerbeau. Atlas-based reduced models of blood flows for fast patient-specific simulations. In O. Camara, M. Pop, K. Rhode, M. Sermesant, N. Smith, and A. Young, editors, *Statistical Atlases and Computational Models of the Heart*, volume 6364 of *Lecture Notes in Computer Science*, pages 95–104. Springer Berlin, 2010.

[36] J. Park, S. Shontz, and C. Drapaca. A combined level set/mesh warping algorithm for tracking brain and cerebrospinal fluid evolution in hydrocephalic patients. In Y. Zhang, editor, *Image-Based Geometric Modeling and Mesh Generation*, pages 107–141. Springer Netherlands, 2013.

[37] B. Raghavan, P. Breitkopf, Y. Tourbier, and P. Villon. Towards a space reduction approach for efficient structural shape optimization. *Structural and Multidisciplinary Optimization*, 48:987–1000, 2013.

[38] T. Richter. *Fluid-structure Interactions: Models, Analysis and Finite Elements*, volume 118. Springer, 2017.

[39] M. Ripepi. *Model Order Reduction for Computational Aeroelasticity*. PhD thesis, , Politecnico di Milano, Italy, , 2015.

[40] G. Romanelli. *Computational Aeroservoelasticity of Free-Flying Deformable Aircraft*. PhD thesis, , Politecnico di Milano, Italy, , 2012.

[41] J. Samareh. Aerodynamic shape optimization based on Free-Form Deformation. In *Proceedings of the 10th AIAA/ISSMO Multidisciplinary Analysis and Optimization Conference*. AIAA, 2004.

[42] T. Sederberg and S. Parry. Free-Form Deformation of solid geometric models. In *Proceedings of SIGGRAPH - Special Interest Group on GRAPHics and Interactive Techniques*, pages 151–159. SIGGRAPH, 1986.

[43] D. Shepard. A two-dimensional interpolation function for irregularly-spaced data. In *Proceedings-1968 ACM National Conference*, pages 517–524. ACM, 1968.

[44] J. Sokolowski and J.-P. Zolésio. *Introduction to Shape Optimization: Shape Sensitivity Analysis.* Springer, 1992.

[45] M. Staten, S. Owen, S. Shontz, A. Salinger, and T. Coffey. A comparison of mesh morphing methods for 3d shape optimization. In *Proceedings of the 20th international meshing roundtable*, pages 293–311. Springer, 2011.

[46] M. Tezzele, F. Ballarin, and G. Rozza. Combined parameter and model reduction of cardiovascular problems by means of active subspaces and pod-galerkin methods. in press, https://arxiv.org/abs/1711.10884, 2018.

[47] M. Tezzele, F. Salmoiraghi, A. Mola, and G. Rozza. Dimension reduction in heterogeneous parametric spaces with application to naval engineering shape design problems. *Advanced Modeling and Simulation in Engineering Sciences*, 5(1):25, Sep 2018.

[48] M. Vaillant and J. Glaunès. Surface matching via currents. In G. Christensen and M. Sonka, editors, *Information Processing in Medical Imaging: 19th International Conference, IPMI 2005, Glenwood Springs, CO, USA, July 10-15, 2005. Proceedings*, pages 381–392. Springer Berlin Heidelberg, 2005.

[49] S. Volkwein. Proper Orthogonal Decomposition: Theory and Reduced-Order Modeling. *Lecture Notes, University of Konstanz*, 2012.

[50] S. Walton, O. Hassan, and K. Morgan. Reduced order mesh optimisation using proper orthogonal decomposition and a modified cuckoo search. *International Journal for Numerical Methods in Engineering*, 93(5):527–550, 2013.

[51] W. Wigley. A comparison of experiment and calculated wave-profiles and wave-resistances for a form having parabolic waterlines. *Proceedings of the Royal Society of London A: Mathematical, Physical and Engineering Sciences*, 144(851):144–159, 1934.

[52] J. Witteveen. Explicit and robust Inverse Distance Weighting mesh deformation for CFD. In *48th AIAA Aerospace Sciences Meeting Including the New Horizons Forum and Aerospace Exposition*. AIAA, 2010.

[53] J. Witteveen and H. Bijl. Explicit mesh deformation using Inverse Distance Weighting interpolation. In *19th AIAA Computational Fluid Dynamics*. AIAA, 2009.